# Atomistic modeling of mechanical behavior ☆

## Ju Li [a,*], Alfonso H.W. Ngan [b], Peter Gumbsch [c,d]

[a] *Department of Materials Science and Engineering, Ohio State University, Columbus, OH 43210, USA*
[b] *Department of Mechanical Engineering, The University of Hong Kong, Hong Kong, PR China*
[c] *Fraunhofer-Institut für Werkstoffmechanik, 79108 Freiburg, Germany*
[d] *Institut für Zuverlässigkeit von Bauteilen und Systemen, Universität Karlsruhe, 76131 Karlsruhe, Germany*

## Abstract

Atomistic modeling plays a critical role in advancing our understanding of microstructure evolution and mechanical properties. We present progresses in the theory and computation of ideal strength, dislocations activation processes and brittle fracture from the atomic perspective, in close connection with experiments and other levels of modeling. New discoveries are often made in the "virtual atoms labs". There, one has perfect control of the simulation conditions, and the amount of detailed atomistic information is often breathtaking. Yet, this information can only be seen, utilized and appreciated in full in light of experiments and models for other length/time-scales.
© 2003 Published by Elsevier Ltd on behalf of Acta Materialia Inc.

*Keywords:* Micromechanical modeling; Elastic instability; Fracture; Dislocation mobility; Thermally activated processes

## 1. Introduction

Parallel to the development in solid-state physics, where computational physics has developed into a respected branch of scientific investigation after classical experiment and theory, atomistic modeling and simulation has become a maturing tool in materials science and particularly for the investigation of the mechanical properties of materials. Several developments in the recent past have made the atomistic approach increasingly more attractive:

- Generic atomistic interaction models have now largely been replaced by improved environment-dependent atomistic interaction models and advanced embedding techniques which allow progressively more subtle quantum mechanical effects to be handled. Besides providing more realistic descriptions of the atomic interaction of pure metals, these techniques now allow the material-specific simulation of semiconductor systems, intermetallics and even first steps towards chemically complex systems.
- Studies of reasonably sized systems for the properties of individual defects and for the interactions between small numbers of defects can today be performed very systematically on desktop computers. Supercomputers have given access to such studies on the basis of direct

quantum mechanical methods and to the investigation of large multi-million atom systems.
- Atomistic techniques are increasingly used as a fundamental basis in multiscale modeling approaches to materials behavior.
- Increasing interest in nanoscale systems and phenomena has led to more interest in the atomistic processes determining the stability and performance of small systems.

In this article, we will certainly not be able to give an overview of all these developments and particularly we will not be reviewing the technical and methodological improvements. Instead we will give a few examples on the different applications of atomistic modeling techniques, in a few areas which we think are representative. These mainly fall in three categories. First, atomistic modeling is now used for the systematic investigation of a particular, often material-specific phenomenon. Examples are the properties and the motion of screw dislocations in body-centered cubic (BCC) metals (Section 3), the structure and the properties of the Kear–Wilsdorf lock in L1$_2$ alloys (Section 3), or the cleavage and the crack propagation direction anisotropy in silicon (Section 4). Second, atomistic modeling is used for the exploratory investigation of complex processes far away from equilibrium. Examples are studies of the nanoindentation of metallic thin films (Section 2) or of the development of the plastic zone at the tip of a crack (Section 4). Third, atomistic modeling is now increasingly applied to systematically study the behavior of certain materials defects under precisely controlled loading or boundary conditions. This knowledge is then often used as input to defect-based larger scale simulations. Such studies involve the dependence of dislocation velocity or crack tip speed on driving force (Section 4) and studies of the strength of dislocation junctions or locks (Section 3).

## 2. Ideal strength and defect nucleation

As devices shrink to the nanoscale, the material's defect population starts to differ significantly from that of the bulk, due to surface

annealing, change of source operating conditions, different synthesis/processing routes, etc. As a result of these and Weibull statistics, an enhancement of low-temperature strength is usually observed. If we follow the above tendency to its limit by letting the bulk defect density approach zero, what strength can the material reach? The ideal strength of a material is defined to be the maximal homogenous stress that a perfect crystal, without structural or compositional defects, can withstand. As such, it is the upper limit to the particular material's strength. The theoretical notion of ideal strength was established early in the last century [1], but only recently—with the advancement of high precision nanoscale instrumentations—do researchers begin to quantitatively probe it. Along with the experimental developments, first-principles calculations and atomistic simulations play a concurrent and critical role in discovering new phenomena and elucidating the underlying mechanisms. Because the relevant phenomena's length- and time-scales now readily overlap in these approaches, the great synergy between them will make this area very exciting in the years to come.

Aside from the practical significances, the ideal strength is also a very fundamental intrinsic material trait much like the elastic constant, and reflects deeply the strength and nature of the underlying chemical bonding [2]. If one thinks of the elastic constant as a good reflection of the stiffness of the bonds when they are distorted slightly, then the ideal strength fundamentally characterizes the bonds when they are stretched to the utmost, that is, the old prime bonds are about to yield, and in the case of shear deformation, new prime bonds are about to form. The breaking and reformation of bonds control the mobility of defects which in turn largely controls the mechanical behavior, even though this happens in a local and asynchronous fashion in a defect, in contrast to the homogeneous and synchronous fashion that bonds break and reform in the ideal strength scenario. But it is precisely the simplicity in a concept or a calculation that imparts value. This aspect of the ideal strength should be emphasized.

Lastly, if the ideal strength is considered to be a static quantity, then mechanical instability would be its dynamic manifestation. Because the phonon modes form a complete basis for all atomic motion

in a perfect crystal at 0 K [3], stability of the phonon modes is a necessary and sufficient condition for the mechanical stability of the perfect crystal at 0 K. In monatomic solids, the phonon modes that first go unstable are usually long elastic waves, in which case we have an elastic instability. In binary compounds and more complicated crystals, phonons other than the elastic waves may become unstable first [4]. This first-principles analysis can be applied to inhomogeneous systems as well: when the translational symmetry is broken by lattice defects, the normal modes can no longer be labeled by a wave vector $\mathbf{k}$, but modal analysis is still rigorously correct at 0 K and there are efficient methods to probe the local soft modes [5]. In any case, the initiation of the instability is controlled by linear eigenvalue (bifurcation) analysis; the final products of the instability are atomistic defects such as microcracks, dislocation loops, twins or martensite embryos. What happens in between, what controls certain defects to be nucleated, and how much one can predict based on the linear instability eigenvectors are the questions that can be addressed using atomistic simulations.

## 2.1. Linear stability analysis

The Helmholtz free energy of a representative volume element (RVE) can be expanded as [6]

$$F(Y) \equiv F(X) + \Omega(X)(\tau_{ij}(X)\eta_{ij} \qquad (2.1)$$
$$+ \ C_{ijkl}(X)\eta_{ij}\eta_{kl}/2 + \cdots)$$

where $\Omega$ is the volume, $\tau$ is the stress and $C$ is the isothermal elastic constant at state $X$, and $\eta$ is the Lagrangian strain of a perturbed state $Y$ with respect to $X$, defined as

$$\eta_{ij} = (u_{i,j} + u_{j,i} + u_{k,i}u_{k,j})/2 \qquad (2.2)$$

in which $\mathbf{u} \equiv \mathbf{y} - \mathbf{x}$ is the displacement, and $\mathbf{x} \in X$, $\mathbf{y} \in Y$ track the same material point. Here, (2.1), (2.2) prescribe a homogeneously strained volume element, so $u_{i,j}$ is a constant. The second-order term $u_{k,i}u_{k,j}$ is necessary because otherwise the $F(\mathbf{R}X) = F(X)$ rotational invariance would only be true to the first-order in rotational matrix $\mathbf{R}$; specifically, the invariance would be broken at the second-order—and linear stability analysis is solely concerned with the second-order terms.

Now imagine that a long elastic wave is excited in the system, $\mathbf{u}(\mathbf{x}) = \mathbf{w}e^{i\mathbf{k}\cdot\mathbf{x}}$. By translational invariance of the perfect crystal this excitation is decoupled from excitations at other wavelengths. Note that $\mathbf{u}(\mathbf{x})$ is a true variational degree of freedom, but $\eta(\mathbf{x})$ is not, so even though in (2.1), the second-order term in $\eta$ is scaled by $C$, the stability is not governed by $C$. Assuming the change in total free energy is the sum of free energy changes in individual RVEs, we have,

$$\Delta F = \int d\mathbf{x}(\tau_{ij}\eta_{ij}(\mathbf{x}) + C_{ijkl}\eta_{ij}(\mathbf{x})\eta_{kl}(\mathbf{x})/2 \qquad (2.3)$$
$$+ \cdots)$$

The second-order $\Delta F$ in $\mathbf{u}(\mathbf{x})$ is then, by plugging (2.2) into (2.3),

$$\Delta_{(2)}F = \int d\mathbf{x}(\tau_{jl}\delta_{ik} + C_{ijkl})u_{i,j}(\mathbf{x})u_{k,l}(\mathbf{x})/2 \qquad (2.4)$$

which, in order to maintain positive definiteness, must satisfy,

$$\Lambda(\mathbf{w},\mathbf{k}) \equiv (C_{ijkl}w_i w_k + \tau_{jl}|\mathbf{w}|^2)k_j k_l > 0 \qquad (2.5)$$

for all polarization vectors $\mathbf{w}$ and wave vectors $\mathbf{k}$. As linear long waves are considered here, $|\mathbf{w}|$ and $|\mathbf{k}|$ are immaterial, and we can take $|\mathbf{w}| = 1$ and $|\mathbf{k}| = 1$. $\Lambda(\mathbf{w}, \mathbf{k})$ divided by the mass density and extremized under the constraint $|\mathbf{w}| = 1$ is in fact the eigenfrequency squared of the long-wavelength phonon. $\Lambda_{\min} \equiv \min_{|\mathbf{w}| = 1,|\mathbf{k}| = 1}\Lambda(\mathbf{w},\mathbf{k})$ then indicates the softest elastic wave(s) existing in the crystal under a particular strain (slope of the softest branch of the phonon dispersion curves near the $\Gamma$-point is proportional to $\sqrt{\Lambda_{\min}}$). When $\Lambda_{\min}$ changes from positive to negative, certain elastic wave(s) changes from oscillatory to exponentially growing in amplitude with time. $\Lambda_{\min} = 0$ then marks the change in stability of a homogeneous crystal. If $\Lambda_{\min} = 0$ is achieved simultaneously by $(\mathbf{w}_\alpha, \mathbf{k}_\alpha)$, $\alpha = 1...M$, which are mutually linearly independent in 6-D vector space, we say the elastic instability is $M$-fold degenerate.

The above analysis is based on a homogeneous, albeit highly strained, perfect crystal. If $\tau_{jl}$ and $C_{ijkl}$ vary slowly spatially compared to the range of the interatomic force constants, we may extend

the analysis to a perfect crystal under an inhomogeneous strain field. By interpreting $\Lambda_{min}$ as a measure of micro-stiffness that varies locally, instability is predicted at the location where $\Lambda_{min}$ vanishes [7]. Direct atomistic simulations indicate that $\Lambda_{min} = 0$ accurately predicts the time and locations of dislocation dipole nucleation in 2-D bubble raft indentation simulations [8].

Before taking a closer look at the instability in the next section, it suffices to say here that the character of $\mathbf{w}_{min}$ and $\mathbf{k}_{min}$ that achieves $\Lambda_{min} = 0$ is an important predictor of the type of atomistic defect to develop. If $\mathbf{w}_{min}$ is more perpendicular than parallel to $\mathbf{k}_{min}$, then the unstable wave is transverse, i.e. it is a soft shear wave. In that case (see Fig. 1), it is very likely that a dislocation loop or a twin embryo would be nucleated; furthermore, $\mathbf{k}_{min}$ is likely to be aligned with the slip plane normal $\mathbf{n}$, and $\mathbf{w}_{min}$ is likely to be nearly parallel to the (partial) Burgers vector $\mathbf{b}$. If however $\mathbf{w}_{min}$ is more parallel than perpendicular to $\mathbf{k}_{min}$, then the unstable wave is longitudinal, and a microcrack is likely to result, with $\mathbf{w}_{min}$ and $\mathbf{k}_{min}$ nearly parallel to the crack plane normal $\mathbf{n}$. This relationship is merely approximate, though, since $\mathbf{w}_{min}$ is just the instantaneous tangent at the inflection point along the transition path, and not the vector directly connecting the initial and final states. Fig. 1 illustrates the so-called shear activation volume effect, which belongs to the class of phenomena just described.
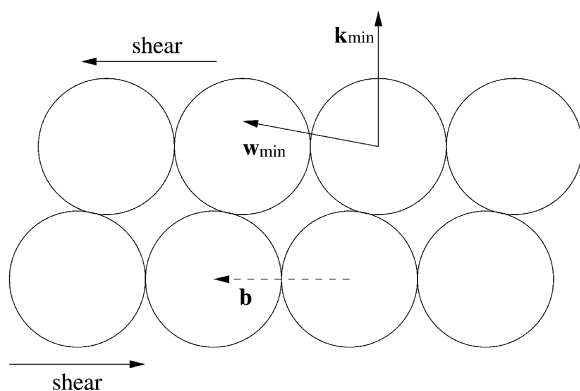


Fig. 1. This illustrates the shear activation volume effect. $\mathbf{w}_{min}$ may have a small angle with the final Burgers vector $\mathbf{b}$, which connects two minima on the energy landscape, since $\mathbf{w}_{min}$ is only the instantaneous tangent direction along the transition path at the inflection point.

Imagine rows of hard-sphere atoms arranged in a close-packed triangular lattice, and a shear stress is applied that will drive the top row atoms to slide to the left. When the stress is gradually increased to a critical level that the top row hard spheres are just about to "roll over", the instantaneous rolling direction is $\mathbf{w}_{min}$. But $\mathbf{w}_{min}$ is not equal to the final overall displacement $\mathbf{b}$, which is the path integral of instantaneous rolling tangents, including those before and after the instability. In plain words, there needs to be some volume expansion before the shear instability, and shrinkage after the instability. In a 2-D bubble raft indentation simulation, there is less than 1° angle difference between $\mathbf{k}_{min}$ and the final slip plane (which is the close-packed plane) normal $\mathbf{n}$, but there is about 12° difference between $\mathbf{w}_{min}$ and $\mathbf{b}$, for the dislocation dipoles nucleated [8].

Discussion about the boundary condition of the variational procedure has been postponed until now, because it is a subtle issue. Certainly, it is straightforward to see that in (2.3), if the system is under Born-von Karman periodic boundary condition (PBC), or fixed displacement condition ($\mathbf{u}|_{\partial\Omega} = 0$), then the above second-order variational procedure is correct. Yet in the real world, the material is often directly coupled to external loading. If external work $\Delta W$ is elicited by $\mathbf{u}(\mathbf{x})$, then we need to add $\Delta W$ to $\Delta F$ to obtain $\Delta G$, and second-order contribution from $\Delta W$ should in general be incorporated. This complicates the problem because we often do not know enough about the loading apparatus to know what the second-order contribution from $\Delta W$ is [6]. Fortunately, in many cases of inhomogeneous strain field this issue can be avoided, for a soft spot $\tilde{\Omega}$ develops inside the sample—a region of negative $\Lambda_{min}$—that is surrounded by materials with positive $\Lambda_{min}$, a "firewall" that isolates $\tilde{\Omega}$ from direct external loading. In such scenarios, the correct strategy for $\mathbf{u}(\mathbf{x})$ to destabilize the system variationally is to be a localized wave pack inside $\tilde{\Omega}$, since it does not pay to try $\mathbf{u}(\mathbf{x}) \neq 0$ within the "firewall". $\mathbf{u}(\mathbf{x})$ will then have no access to the external work, and the Helmholtz free energy analysis is correct.

## 2.2. *Homogeneous defect nucleation*

The products of homogeneous nucleation are atomistic defects. Yet, the analytical criterion developed in the last section only deals with the stability of long elastic, or continuum waves. How does an unstable continuum wave evolve into atomistic defects, which are regarded as singularities at the continuum level? We propose the following four-stage process:

I Linear growth of the unstable elastic wave, $\mathbf{u}(\mathbf{x},t) = \mathbf{w}_{\min}e^{i\mathbf{k}_{\min}\cdot\mathbf{x} - i\sqrt{\Lambda_{\min}}t}$, well described by the continuum. The initiation of the linear instability is controlled by $\Lambda_{\min} < 0$. During this stage the wave grows in amplitude but its shape (wave form) maintains, as all linear waves do.

II When the wave amplitude grows to a certain level, non-linear terms in the Hamiltonian start to have an effect, which distort the wave form to have an ever steepening front like sea waves approaching the shore. But during this stage, the continuum picture and the continuum Hamiltonian still work because the width of the steepening wave front is still much greater than atomic lattice spacing.

III The wave front continues to steepen, to the point that its width approaches atomic spacing. Now we must transfer its description, at least for the wave front part, from the continuum to an atomistic (discrete) description. What then develops is an atomistically sharp shock front—which could either be a shear shock or a longitudinal (sound) shock.

IV As the length scale of the wave front shrinks, ruggedness of the atomistic potential energy landscape becomes visible. The energy that has been transported from the rest of the strained material to the wave front now is dissipated as the discrete atomic layers in the shock get "dragged" over the crests and valleys of the energy landscape, and is converted to heat. Eventually, the shock is trapped and arrested in a low-dimensional atomistic energy landscape. The stationary shock is the nucleated defect. A dislocation, for instance, is nothing other than the bounding rim of a one-layer shear shock.

The above four-stage evolution of an unstable

elastic wave has been confirmed by direct molecular dynamics simulation. Fig. 2 shows a 2-D model solid whose atoms interact via a Morse potential with exponent 3.5. The supercell under PBC is oriented such that its *x*-axis is along the slip plane normal **n** and *y*-axis is along the Burgers vector **b**. The cell dimension is $L_x = 100$ atomic layers, $L_y = 9\mathbf{b}$. A uniform shear strain is applied to the entire supercell at temperature $T = 0$. Then, a perturbational elastic shear wave whose wavelength spans the entire $L_x$ (the smallest **k** possible) is injected into the system. The amplitude of the shear wave is initially very small, only 0.002**b**. The ideal shear strain of this crystal has been determined previously to be around 0.21 at low-*T*, from the cusp in the overall strain–stress response. We find that when the overall strain is less than 0.21, the injected perturbational shear wave manifests oscillatory behavior with time. As the overall strain applied approaches 0.21, the oscillation gets slower and slower in frequency. At an overall shear strain of 0.215, the perturbational shear wave shows no time-oscillations at all and subsequently undergoes Stages I–IV. Fig. 3 shows the wave profiles at reduced times $t = 0$, 75.6, 112 and 122.8. From $t = 0$ to 75.6, the evolution is in Stage I, as the wave amplitude grows from 0.002**b** to 0.01**b**, but the wave shape does not change. This is related to the fact that all linear equations like $\ddot{\gamma} = \gamma$ are symmetric with respect to $\gamma \mapsto -\gamma$, so it cannot distinguish between positive strain perturbation (incremental strain of the same type as the overall strain) and negative strain perturbation (incremental strain opposite to the overall strain). And since the initial sinusoidal wave form is symmetric in its positive and negative incremental strains, this symmetry maintains as long as the linear equation is valid.

From $t = 75.6$ to 112, the amplitude continues to increase, but the wave shape also starts to change, with the positive incremental strain part becoming *more and more localized*. For this to happen, we need to have terms like $\gamma^2$ added to $\ddot{\gamma} = \gamma$, breaking the $\gamma \mapsto -\gamma$ symmetry. As one can see, the wave form is no longer symmetric at $t = 112$, with the positive strain part having a smaller "wavelength" than the negative strain part. Nevertheless, during this period (Stage II) the entire kin-
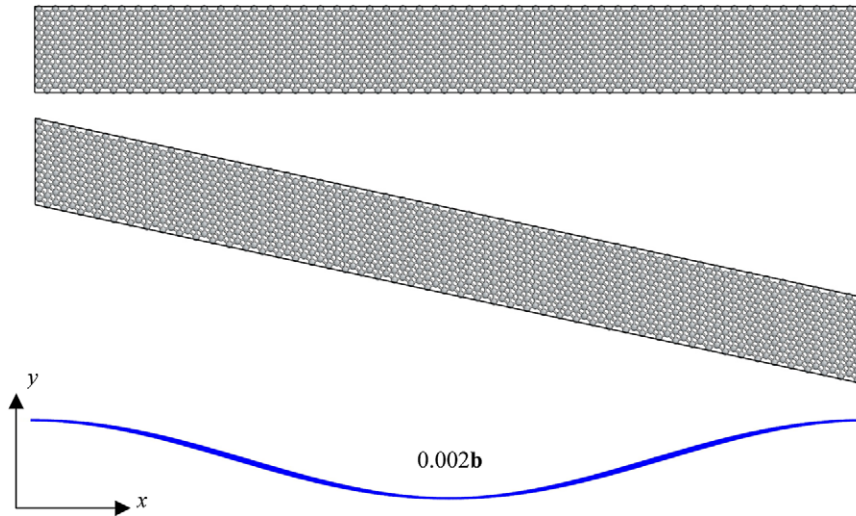
Fig. 2. A 2-D solid with atoms interacting via the Morse potential. $x$-Axis is the close-packed plane normal direction ($L_x$ = 100 layers), $y$-axis is the Burgers vector direction ($L_y$ = 9$b$). The supercell is first subjected to uniform shear, and then a monochromatic long shear wave of amplitude 0.002$b$ is put in the system. If this perturbational long wave is stable, it will be oscillatory with time. But if it is not, it will go through the four stages, and an atomistically sharp shear shock will form.

ematics can still be described within the continuum framework.

From $t$ = 112 to 122.8, the front steepening progresses to a point that it is no longer appropriate to describe the positive incremental strain part by a smooth profile, as just a few atomic layers absorb most of the positive incremental strain. In this "transfer" stage, Stage III, one must hand over the shock front description from a continuum one to an atomistic one. A genuine, atomistically sharp shock is forming, whose local strain is of the *same* character as the overall applied strain. At $t$ = 122.8, the wave amplitude is still just ~0.05$b$, but because it is distributed just between a few layers, the displacement between two adjacent atomic layers is becoming quite significant, and the system starts to truly traverse the atomistic energy landscape.

Fig. 4(a) shows the generalized stacking fault (GSF) energy surface of face-centered cubic (FCC) Cu, computed using the Mishin potential [9]. One can map the relative shear displacement between one atomic layer and the next adjacent layer, on the GSF. The 100 atomic layers in the supercell then map to 100 points on the GSF surface. Before the critical strain is reached, all these displacement

points are bunched together on the GSF and a perturbational wave cannot disperse them. After the critical strain is reached, and elastic instability occurs, a *bifurcation* happens, in which most of the points start to go in one direction (relaxing back toward the origin—the negative incremental strain part of Fig. 3 profiles), and just a few displacement points start to go the opposite way (the positive incremental strain part of Fig. 3 profiles). In fact, since the total displacement is a constant, set by the supercell PBC strain, the *center of mass* of the 100 points on the GSF is fixed. So in order to compensate for the backward relaxation displacements of most of the points, the few runaway points must traverse the GSF from hill to valley to hill … and during this bumpy ride the incoming energy will be dissipated into heat. Fig. 4(b) shows the final, arrested incremental displacement profile, in which the wave amplitude has grown to 12$b$. Even more remarkable is that about 8$b$ of the 12$b$ is taken up by just one point on the GSF, that is, the relative shear displacement between one pair of adjacent atomic layers.

Why is the four-stage strain localization process energetically favorable? This is clear when we add the final incremental displacement profile (Fig.
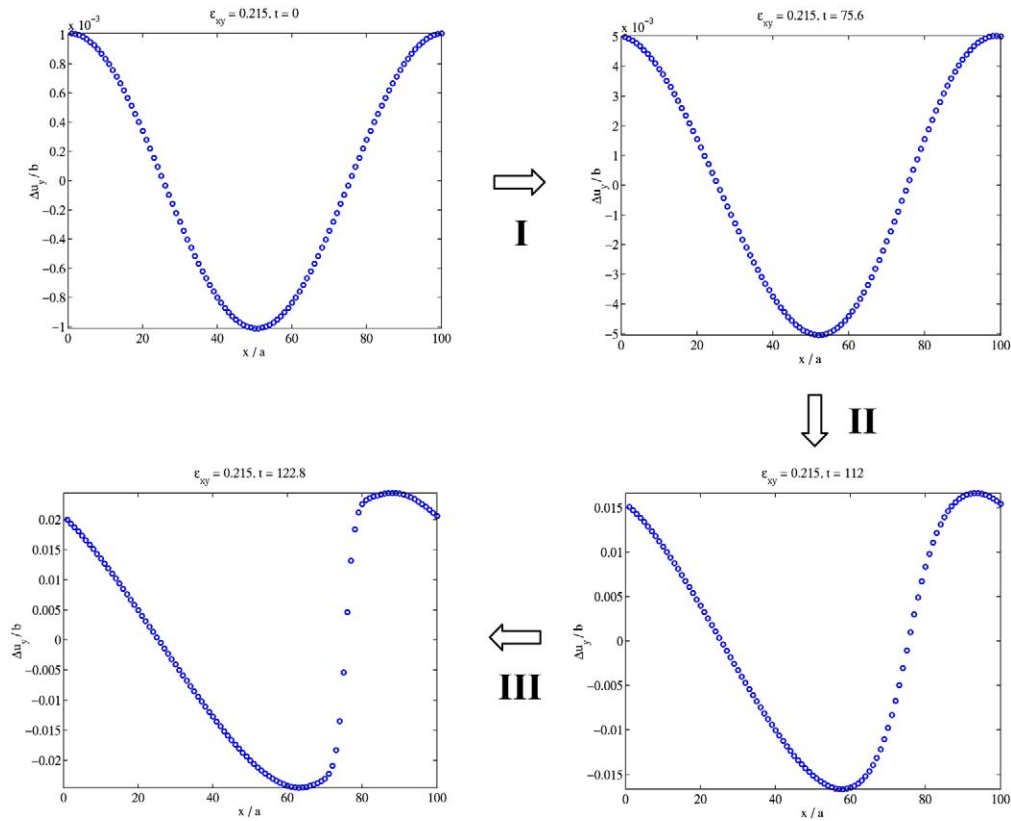
Fig. 3.   Stages I–III of the unstable evolution of the long wave shown in Fig. 2. A circle denotes the shear displacement of one atomic layer, normalized by the Burgers vector **b**.

4(b)) grown from the perturbational long wave, to the overall PBC uniform strain/displacement (Fig. 4(c)). The result is Fig. 4(d), the final, total displacement. The point is that the final state (Fig. 4(d)) has a lower potential energy than the initial state (Fig. 4(c)). In (c), the strain energy is distributed uniformly. In (d), the strain energy is somewhat relaxed in all parts of the supercell except in the shock region. Because the total displacement is fixed, these relaxations must be absorbed by the thin shock, and indeed the shock region may have a higher energy than before. However, since the GSF energy is a periodic function in the shear displacement **x**: **x** + **b**, **x** + 2**b**, **x** + 3**b**, etc., have the same GSF energy. Especially, **x** = **b**, 2**b**, 3**b** have vanishing GSF energy. By *condensing* the total shear displacement to between just two atomic layers, the total energy is reduced. This is the fundamental reason behind converting the affine strain

energy $\gamma_\infty(\mathbf{x})$—the most delocalized strain energy, to the GSF energy $\gamma_1(\mathbf{x})$—the most localized strain energy [2], through strain localization process. The nucleation and mobility of dislocations is a scheme that nature deploys to achieve this fundamental purpose.

Analogous to the Big Bang model of the beginning of the universe, we see that entire sequences of events could unfold within a very short time after the elastic instability. But because it is related to the origin of defect species, a careful examination is warranted. For instance, one could propose that a twin embryo forms if the steepening shear shock can be trapped by the three-layer multiplane generalized stacking fault (MGSF) [10] in BCC metals. If no MGSF can trap the steepening shock front, and if it progresses down to one layer and eventually gets trapped by the single-layer GSF, then we get a dislocation loop. The nature of this
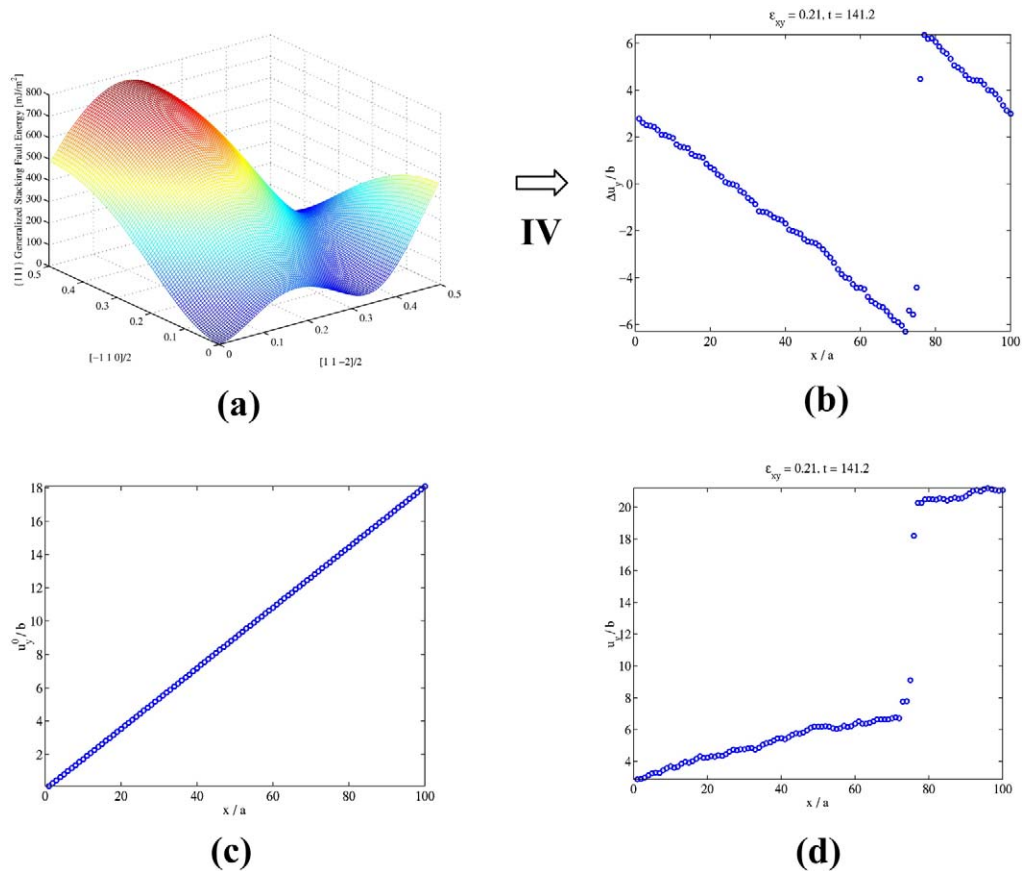
Fig. 4. (a) One-layer generalized stacking fault (GSF) energy of FCC Cu calculated using the Mishin potential [9]. (b) Final stationary product of the unstable elastic wave in Fig. 2, after Stage IV evolution. Notice that this is the incremental displacement profile, which must be a periodic function. (c) Displacement caused by the uniform supercell strain. (d) Total final displacement profile by summing (b) and (c).

instability dynamics then becomes an entry point for ascertaining which crystallographic systems should be twinning systems and which should be slip systems, by correlating the observed dynamics with the attraction basins, saddle-points and bifurcation transitions of the low-dimensional atomistic energy landscapes. The proposed theory has been preliminarily corroborated by direct atomistic simulations in the case of BCC Mo using the Finnis–Sinclair potential [11], in a quasi-1-D chain model similar to the above.

### 2.3. Nanoindentation and incipient plasticity

Modeling and experiments of nanoindentation of thin film materials [12] provide a good testing

ground for studying the ideal strength, defect nucleation—both homogeneous and heterogeneous, and incipient plasticity. The Hertzian solution of 3-D spherical indentation of linear elastic half space [13] provides a global view of the stress distribution and indicates that the spherical indenter acts like a lens, which projects the maximum shear stress to an internal point (the "focus") a finite distance away from the surface. This favors stress-driven instabilities occurring first in the bulk, and minimizes the influence of surface defects, which makes the study of ideal strength—a bulk characterization—possible.

Direct MD simulation of 3-D spherical indentation into a flat Al (1 1 1) surface [8] verifies that homogenous dislocation nucleation indeed occurs.

Furthermore, the homogenous nucleation site is at a depth $z$ equal to 51% of the contact radius $a$, in good agreement with the depth of $0.48a$ predicted by the Hertzian solution. But the nucleation site is also significantly off-axis, at a radial distance $r \simeq 0.5a \simeq z$ away, a feature that is first revealed by atomistic simulations [14]. This is probably because the elastic instability is driven more strongly by slip-system specific resolved shear stress than the von Mises shear stress invariant. Quantitative $\Lambda_{min}$ analyses have been performed by Zhu et al. [15] for 3-D spherical indentation into flat Cu (1 1 1) surface, based on the Mishin potential [9] and checked against ab initio calculations. They find that the homogeneous nucleation sites are at $z = 0.61a$ and $r = 0.58a$, and threefold symmetric to the $\langle 1\,1\,1 \rangle$ indentation axis.

Because the initiation of elastic instability is stress-driven and governed by a continuum criterion, it is amenable to the finite element approach, provided a fully non-linear treatment is used, which includes a constitutive relation that is faithful to the atomistic potential model at large strain. The so-called interatomic potential-based finite element method (IPFEM) [7,8,15] is a sub-feature set version of the quasicontinuum method [16] and is in fact a simple numerical implementation of hyperelasticity with the Cauchy–Born hypothesis [17]. It involves on-the-fly embedding of atomistic lattice sums in general purpose finite-element software packages such as ABAQUS. By comparison with fully atomistic results, it is verified that IPFEM is very accurate down to indenter radius ~10 nm and system size ~200,000 atoms [8,15]. Because the FEM can make use of adaptive meshing, this allows one to model stress distribution in systems with much more complicated boundary conditions (Berkovich indenter, oxide layer, substrate effect, etc.) efficiently. Currently, IPFEM is limited to modeling nanoindentation up to the point of elastic instability, and making predictions with respect to the critical load/displacement, homogeneous nucleation site, $\mathbf{w}_{min}$, $\mathbf{k}_{min}$ and consequently characters of the defect to be nucleated (slip plane and Burgers vector). It cannot yet follow the nucleated defect through the incipient plasticity development. The hope is that in the future one will be able to model

microstructure evolution and incipient plasticity under nanoindentation by combining IPFEM with analytical defect nucleation criteria and with dislocation dynamics (DD) modeling [18–21].

Currently, the microstructural evolution underneath a nanoindenter is modeled mainly by direct atomistic simulations. A central topic of such simulations is trying to understand the distribution of displacement excursions in load-controlled indentation experiments [8,22,23]. It was realized that while some of the so-called "minor bursts" consist of displacement excursions on the order of nanometers; other so-called "major bursts" manifest displacement excursions on the order of tens of or even a hundred nanometers. Simple estimates indicate that the "major bursts" could not possibly all correspond to homogenous dislocation nucleation, and suggest instead the formation of dislocation sources similar to the Frank–Read source beneath the indenter—whose operating stress is far below the initial local stress, which will then allow for the heterogeneous nucleation of hundreds of dislocation loops in one time without the need of an indenter load increase. The transition from homogeneous dislocation nucleation to source formation and then to prolific heterogeneous dislocation nucleation is the main conclusion of our atomistic modeling [7,8], although the full picture is still far from clear. In the spherical indentation of an aluminum (1 1 1) surface, a sessile dislocation structure quickly develops beneath the indenter after the homogeneous nucleation. Some time later, a highly mobile prismatic dislocation loop, with the aid of the sessile structure as pinning points, is emitted from beneath the indenter, as shown in Fig. 5. Prior to that, homogenous dislocation nucleation has yielded only expanding glide loops on single slip planes; the formation of a prismatic loop requires the cooperative activation of two different slip systems, and therefore can only be produced from a heterogeneous source. This highly mobile prismatic loop then glides through the thin film without any resistance, and exits the free surface at the bottom, leaving behind a slip line parallelepiped. Subsequently, many more prismatic loops are nucleated in this and two other symmetric prism directions, con-
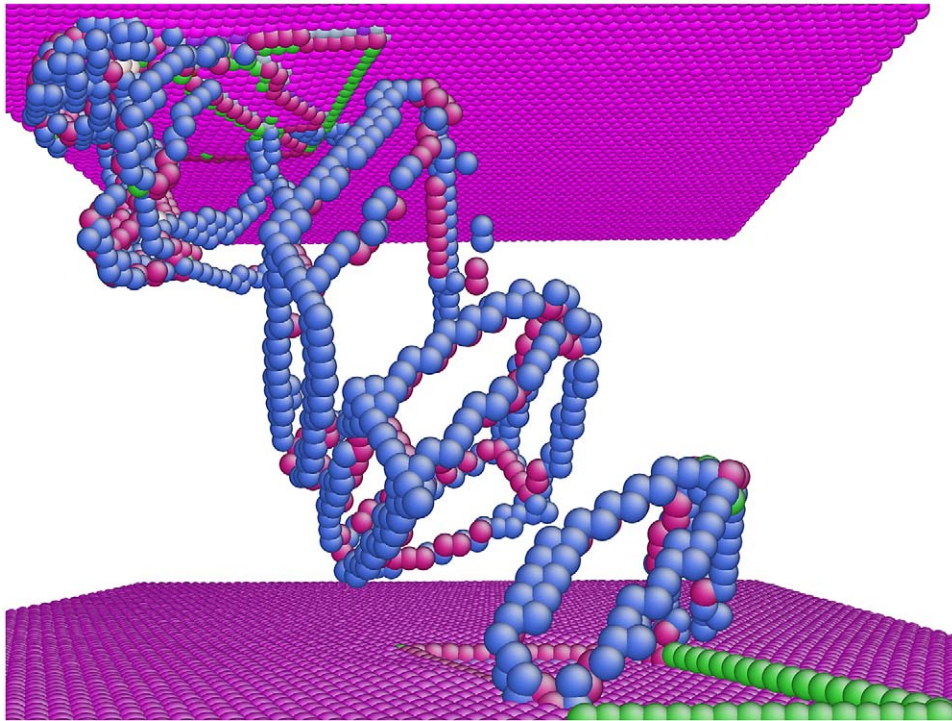
Fig. 5. Concatenated snapshots of a heterogeneously nucleated prismatic dislocation loop gliding through an aluminum thin film in molecular dynamics simulation of its (1 1 1) surface nanoindentation. Only atoms with coordination numbers different than 12 are shown. Each of the four sides of the prismatic loop is a full $1/2<1 1 0>$ dislocation, which is further split slightly into two partial dislocations.

firming the operation of three heterogeneous prismatic dislocation loop sources.

Fig. 6 shows a large-scale molecular dynamics simulation consisting of 2-million aluminum atoms. In such studies, analysis of atomistic data and utilization of visualization tools are critically important. A portable and efficient visualization program, AtomEye, has recently been developed [24]. The film is 41 nm × 41 nm × 20 nm, and the indenter tip radius is 13 nm. The speed of the indenter is 30 m/s, which is certainly very fast for the development of plasticity but is much smaller than the sound speed and therefore still allows for the equilibrium of elastic stresses. After the triggering event of homogenous nucleation, the dislocation density grows rapidly and within 100 ps after contact starts to form an intricate network of dislocations under the indenter, which corresponds to a rudimentary plastic zone. Two main categories of dislocations are observed: those of limited

mobility—either because they are sessile or tied down by the network—and those of basically unlimited mobility, the "runaway" dislocations. Even though the runaway dislocations only make up a small fraction of the total dislocation density, they seem to carry most of the plastic strain. Principal among the runaway dislocations are the threading dislocations connecting the top and bottom surfaces, and prismatic dislocation loops (slip lines on the bottom surface clearly indicate the operation of three symmetric prismatic dislocation loop sources). Conditions for the runaway phenomena exist because once a mobile dislocation moves to the edge of the entangled dislocation network and breaks free from the crowd, the FCC perfect crystal provides very little lattice resistance and they can move on forever until they exit or pile up on the boundary. On the top surface we see the indenter crater, and slip lines indicating cross-slip.
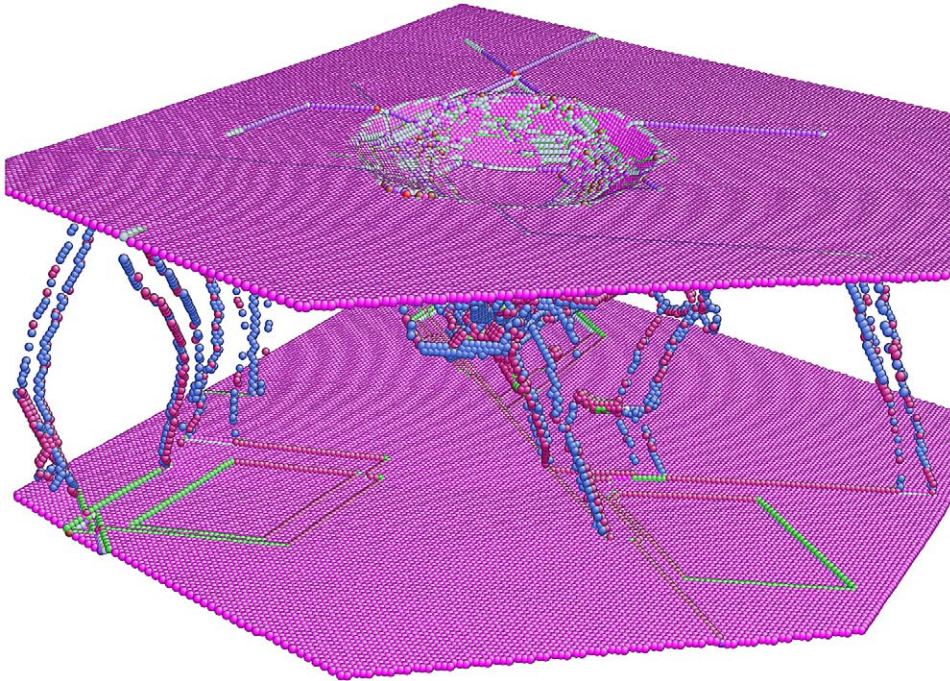
Fig. 6. Microstructural development in a 2-million atom molecular dynamics simulation of nanoindentation of an aluminum thin film. Operations of three equivalent sources of prismatic dislocation loops results in parallelepiped slip lines on the bottom surface. Through-thickness threading dislocations have also been nucleated in the film. Only atoms with coordination numbers different than 12 are shown.

We have carried out similar indentation simulations of FCC Cu and BCC Fe, and observed quite distinct microstructural features. In FCC Cu, there is no dislocation cross-slip and less prismatic loop activity; on the other hand, we have observed heterogeneous nucleation of twin bands and subsequent layer-by-layer thickening growth during nanoindentation. In BCC Fe, we have observed very interesting material pileup and faceting behavior at the top surface near the indenter crater. The influence of temperature, point-defect diffusion and preexistent microstructures like phase or grain boundaries are under investigation by atomistic modelers. New phenomena of nanoindentation, such as delayed pop-in effects [25], are still constantly being revealed experimentally.

It is noted that nanoindentation of metals is only one part of a broad spectrum of nanoscale active-probe experiments and material systems. Nanoindentation of silicon [26], for example, has revealed multiple-stage martensitic transformation, solid-state amorphization, dislocation nucleation and microcrack nucleation in one experiment, in different zones radiating from the indenter crater. Atomistic simulations [27] play a critical role in unveiling and interpreting this rich family of behaviors, concurrent with the experiments.

From the perspective of plasticity theory development, nanoindentation induced incipient plasticity constitutes a grand challenge, as it is characterized by large dislocation density gradients in both space and time, and is therefore a good test case for any size-dependent plasticity theory. Combining this with the first-principles, quantum mechanical evaluation and interpretation of ideal strength [2,15], phonon instability and the origin of atomistic defects, it is a fertile ground for experimentalists, theoreticians and modelers alike.

## 3. Dislocation processes in BCC metals and intermetallics

Dislocation mobility is a vast subject. It is also an area where atomistic modeling has made tremendous impact, since dislocation core structures and atomic-level activation processes govern the mobility and often the macroscopic mechanical behavior. Empirical potential-based atomistic simulations are able to directly model fully 3-D activation configurations (such as cross-slip [28] and kink-pair nucleation [29])—a task which currently stretches the capability of ab initio calculations. The accuracy of the results, however, critically depends on the quality and transferability of the empirical potential. Fitting to different kinds of ab initio energy surfaces is how such empirical potentials are most often constructed. This information flow from ab initio energy surfaces to activation energies is alternatively achieved by Peierls–Nabarro type [30] and phase-field [31] models, which allow for parametric studies, and are generally highly valuable tools for the development of basic understanding, including the interpretation of atomistic results.

Schmid's law states that dislocation glide on a given slip system, defined by the slip plane and the direction of slip, commences when the magnitude of the resolved shear stress on that system reaches a constant critical value. Implicitly this assumes that other components of the stress tensor than shear resolved in the slip plane in the slip direction do not play any role in the deformation process. Furthermore, the critical stress must be independent of the sense of shear. These assumptions are generally valid in metals with close-packed crystal structures for which Schmid's law was originally established. In contrast, BCC metals (see, for example, [32,33]), many intermetallic alloys (see [34]) and some ceramics (e.g. [35]) clearly deviate from the Schmid law. This is usually an indication that dislocation core effects are important. Atomistic modeling and high resolution transmission electron microscopy in these cases often show non-planar core structures for the screw dislocations or even more complicated core dissociations (see, for example, [34,36–38] and references therein). We are not in the position to review all this work and

will rather give a few recent examples in the modeling of dislocation processes in BCC metals and intermetallics, and even within which we cover just a small part of the entire spectrum of dislocation modeling currently performed. Interested readers are encouraged to follow the more general references [39,40].

### 3.1. Glide processes of screw dislocations in BCC metals

In recent years, there has been a renewed interest in studying cross-slip of screw dislocations in the simple FCC structure. As reviewed by Püschl [41], new developments in both linear elastic semi-continuum modeling as well as in the application of atomistic simulation have been made in the past decade or so to investigate the 3-D problem of cross-slip of screw dislocations in the simple FCC structure. This section serves to address parallel developments, both in semi-continuum approaches and in 3-D atomistic simulations, in modeling the cross-slip of screw dislocations in the BCC structure.

### 3.1.1. Background of kink-pair processes in BCC metals

Comparing with close-packed structures, the deformation characteristics of BCC crystals are unusual in terms of the following aspects:

(i) The slip behavior in BCC crystals violates Schmid's law, i.e. the critical resolved shear stress is not a constant, but varies with the orientation of the deformation axis.

(ii) Slip does not take place on definite, low index crystallographic planes, but can occur on any slip planes of the $<1\ 1\ 1>$ zone. The slip pattern is usually wavy.

(iii) The Peierls stresses of BCC metals are in the range of $10^{-2}$ to $10^{-3}\mu$ ($\mu$ being the shear modulus). These are two to three orders of magnitude higher than that of FCC or HCP metals.

(iv) The flow stress of BCC metals increases sharply and exhibits strong strain-rate sensitivity at low temperatures.

(v) Experimental measurements of the activation

volume for slip indicate that the activation process may undergo a change in mechanism as temperature increases. The activation volume increases from $<10b^3$ ($b$ being the $1/2<1\,1\,1>$ Burgers vector) at low deformation temperatures to $>10^2 b^3$ at high temperatures.

(vi) BCC metals usually exhibit a brittle-to-ductile transition (BDT).

These unusual characteristics have triggered a large volume of theoretical investigations at the dislocation level over the last half-century. Hirsch was among the first to suggest that the intrinsic high Peierls stress of BCC metals is due to the non-planar spreading of screw $1/2<1\,1\,1>$ dislocations, in a way conformable to the crystal symmetry about the screw axis [42]. The idea that a $1/2<1\,1\,1>$ screw dislocation in a BCC crystal may dissociate into fractional dislocations forming a non-planar structure was first pursued by Hirsch and Duesbery [43,44]. Central to this "dissociation" theory is the assumption that the fractional dislocations have Volterra-type strain fields connected to one another via stacking faults with constant fault energy. Fault energies were not generally available at the time, and they were regarded as fitting parameters. The theory took detailed crystallographic features into account and was rather successful in explaining qualitatively the orientation and thermal dependence of the critical resolved shear stress. In particular, motion at finite temperatures via kink-pair formation and expansion was investigated by this theory. The results have led to the classical concept [43–46] that different regimes dominate at different temperatures. In the low temperature or high stress regime, it is the nucleation of an opposite-signed kink-pair from the screw dislocation line that forms the activation process. In the high temperature or low stress regime, the activation process consists of the overcoming of the long-range elastic attraction of the two opposite kinks by the applied stress. The activation energy decreases with the applied stress in a rather complex manner. At yet higher temperatures, classical obstacle interaction dominates and the flow stress becomes less temperature and strain

rate sensitive—often referred to as the athermal regime.

Quasi-2-D atomistic simulations, first due to Duesbery et al. [47], were used to study the characteristics of the ground state configuration and motion of screw dislocations that are infinitely straight. The concepts derived from these investigations have now been widely regarded as classical, and the relevant literature has been reviewed by several authoritative authors [48–53]. The earlier simulations were done using empirical potentials not specific to given materials (e.g. Vitek's J-series potentials). One main aim of these initial efforts was to identify common trends among different potentials and if any existed, they were taken as structural consequences of the BCC lattice rather than those of the potentials themselves. It was within the last one or two decades when more accurate material-specific potentials became available. These have allowed a wider range of BCC transition metals to be calculated, and specific behavior of certain groups of metals may now even be identified from ab initio calculations [54,55].

In short, topics (i)–(iii) above have been frequently addressed by 2-D atomistic simulations. However, dislocation motion at finite temperatures is expected to take place via kink-pair mechanisms, and hence these 2-D results may not be directly relevant. Points (iv) and (v) have been traditionally treated by line tension models, incorporating at times crystallographic features derived from Hirsch's Volterra picture of core dissociation. However, the use of ill-defined input parameters such as inner cut-off radii and constant stacking fault energies have inevitably limited the credibility of these models.

The last few years have seen two new aspects of development in modeling kink-pair problems in BCC metals. The first is the development of a semi-continuum approach derived from the classical Peierls–Nabarro (P–N) model [56–60]. The second concerns new 3-D atomistic simulation methods [61–63]. These results have led to more coherent understanding of the kink-pair activation problem, and will be reviewed below.

### 3.1.2. Generalized Peierls–Nabarro models

It is beyond any doubt that atomistic simulation is a powerful tool to predict subtle features of dislocation cores in specific materials. However, there is still some attraction in discussing common trends through a more generic model, because the unusual phenomena listed in Section 3.1.1 above are material and therefore potential independent. One starting point is the Peierls–Nabarro model, which couples the linear elastic response of the major portion of the core to the stacking-fault-like shearing on the slip plane that takes up a major part of the Burgers vector content. The GSF on the slip plane is associated with a non-linear force law known as the γ-surface and can be computed using atomistic means for specific materials.

The original Peierls–Nabarro model was for planar core spreading, but Kroupa and Lejcek [56] first modified the model to make it applicable to the situation of threefold spreading resembling a screw core in the BCC structure (Fig. 7). Ngan [57,58] generalized the original Peierls–Nabarro model into the situation of *n*-fold spreading for a screw dislocation. For any fold of dissociation *n*, explicit integral expressions of the strain and misfit energies have been derived in terms of the relative boundary displacements at the misfit planes, as in the original Peierls–Nabarro model for the planar case. Minimization of the energy then yields the ground state properties of the core. The first success of this model is its ability to explain why a
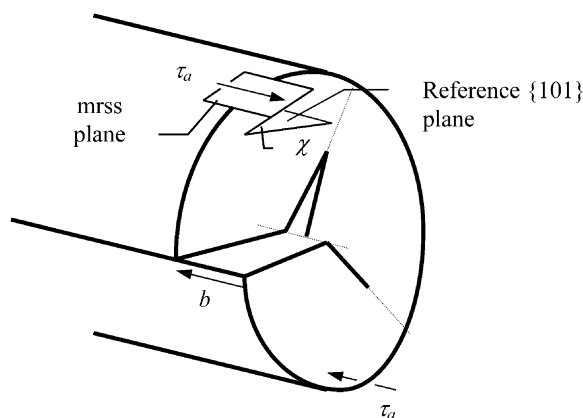


Fig. 7. Threefold dissociated screw dislocation core as depicted in the generalised Peierls–Nabarro model [57,58].

screw dislocation would prefer to dissociate into a non-planar configuration while crystal symmetry does not prevent planar dissociation. Assuming a simple Frenkel-type γ-surface [1], the energy of an *n*-fold dissociated screw dislocation was found to be [57]:

$$E \approx \frac{\mu b^2}{4\pi} \ln\left(\frac{\alpha R_o}{b}\right), \tag{3.1}$$

where the inner cut-off parameter $\alpha$ was estimated by a Rayleigh–Ritz approximation to be

$$\alpha \approx \frac{ne}{2^{2/n-1}\pi} \int_0^\infty \sin\left[\frac{2\pi}{n} - \frac{4}{n}\tan^{-1}(x^{n/2})\right] \frac{x^{n/2}}{1+x^n} dx,$$

which is a monotonically decreasing function of *n*. Here, $R_o$ is the outer cut-off radius, and *e* is the base of the natural logarithm. From the cut-off parameter in Eq. (3.1), a core would therefore lower its energy simply by dissociating into as many folds as crystal symmetry would allow. It thus appears that a sixfold core as observed in group VB metals is more stable than the threefold core as observed in other materials. The more usual threefold state could be the result of deviation of the γ-surface from the Frenkel sinusoidal form. Duesbery and Vitek [52] have indeed found that the γ-surfaces of group VIB metals exhibit "shoulders" at roughly the *b*/3 and 2*b*/3 positions. The shouldering of the γ-surfaces may be a stabilizing factor for threefold cores but more investigation is required to confirm this.

The approximate result in Eq. (3.1) predicts that a planar core (with *n* = 2) would have an energy higher than that of a threefold core (with *n* = 3) by an amount $\Delta E \approx 0.014\mu b^2$, and a more refined calculation [58] shows that $\Delta E$ is likely to be as high as $0.03\mu b^2$. Assuming that the core would become mobile when the threefold configuration shown in Fig. 7 has transformed to a planar configuration by retracting spreading on two slip planes and extending that on the third plane, the rise in energy $\Delta E$ would account for the intrinsic high Peierls stress. More specifically, the Peierls stress required to produce this transformation has been shown to be given by [59,60]

$$\tau_{\mathrm{p}} = \quad\quad\quad\quad\quad\quad\quad\quad\quad\quad (3.2)$$

$$
\begin{cases}
\dfrac{2\Delta E}{A^{*}\cos^{2}\chi} & \text{for eventual slip on a } \{1\,0\,1\} \text{ plane (i.e. } J_2 \text{ behavior)} \\[2mm]
\dfrac{2\Delta E}{A^{*}\cos^{2}(|\chi|-30^{\circ})} & \text{for eventual slip on a } \{1\,1\,2\} \text{ plane (i.e. } J_1 \text{ behavior)}
\end{cases}
$$

where $A*$ is an effective activation area of the applied stress and is of the order of a few $b^2$, and $\chi \in (-30^{\circ}, +30^{\circ})$ is the angle between the maximum-resolved-shear–stress plane and the nearest $\{1\,0\,1\}$ plane (see Fig. 7). Thus, the intrinsic orientation dependence of the Peierls stress is predicted. Within the allowable range ±30° for $\chi$, $\tau_{\mathrm{p}}$ is about $10^{-2}\mu$, which is of the order of magnitude observed experimentally. $\Delta E$ and $A^*$ should depend on whether the slip planes are of $\{1\,0\,1\}$ or $\{1\,1\,2\}$ type, and the variation can be predicted using the appropriate γ-surfaces for the two types of planes. The case of spreading and slip on $\{1\,0\,1\}$ and $\{1\,1\,2\}$ may be referred to the $J_2$ and $J_1$ behavior, respectively, referring to Vitek's original work [47,48]. Focusing only on the variation with load orientation, for the $J_2$ behavior, $\tau_{\mathrm{p}}$ shows a minimum at $\chi = 0^{\circ}$ and a maximum at $\chi = \pm 30^{\circ}$ (see Fig. 8). Such a $\tau_{\mathrm{p}}$–$\chi$ relationship agrees indeed with what is observed in Fe and Mo [50]. The magnitude of variation of $\tau_{\mathrm{p}}$ from $\chi = 0^{\circ}$ to $\chi = \pm 30^{\circ}$ estimated by Eq. (3.2) is ~$10^{-3}\mu$, which again agrees very well with experimental results for Fe and Mo. For the $J_1$ behavior, the slip plane changes from the twinning $\{1\,1\,2\}$ to the anti-twinning $\{1\,1\,2\}$ as $\chi$ increases from $-30^{\circ}$ to $+30^{\circ}$. Atomistic simulations predicted an asymmetry that the twinning slip is easier than the anti-twinning slip; the actual $\tau_{\mathrm{p}}$–$\chi$ variation for $J_1$ may therefore skew towards the $\chi = 30^{\circ}$ side as shown in Fig. 8(c). This twinning/anti-twinning asymmetry was observed in the slip behavior of Ta, Li-Mg, AgMg and β-CuZn [50]. At a first glance, Eq. (3.2) seems to predict symmetric behavior about $\chi = 0^{\circ}$ but it must be remembered that $\Delta E$ and $A^*$ depend on the shape of the γ-surface which is not symmetric with respect to the sense of shear on the $\{1\,1\,2\}$ plane.

Kink-pair mechanisms have also been modeled using a slab approximation [59,60] as illustrated in Fig. 9. Here, plane-strain slabs each representing a certain partially recombined state along the dislocation line are "glued" together and their interactions considered using linear elasticity. Energy functional of the kink-shape can then be obtained and this when minimized will yield the saddle point properties of the dislocation. It was found that similar to the classical prediction by Hirsch and Duesbery, kink-pair nucleation is the activation process at low temperatures while kink-pair expansion dominates at high temperatures. Fig. 10 shows the predicted relation between the combined activation energy $H$ and the applied stress $\tau_{\mathrm{a}}$. It can be seen that $H$ for both regimes approximately obeys the very simple relation

$$H \approx 0.1(1-t)^2 \mu b^3, \quad\quad\quad\quad\quad (3.3)$$

where $t = \tau_{\mathrm{a}}/\tau_{\mathrm{p}}$. Note that $H$ depends on orientation as $t$ is dependent on $\tau_{\mathrm{p}}$. Also shown in Fig. 10 are the experimental results for potassium [64] and high-purity iron [65]. In these two materials $H$ has been measured over a wide temperature range down to liquid helium temperature. The agreement with Eq. (3.3) irrespective of materials and orientation is very impressive.

To summarize, a number of simple relations concerning complicated phenomena such as the intrinsic orientation dependence of Peierls stress and kink-pair activation have been derived from the generalized Peierls–Nabarro model. These relations were derived using simplifying approximations such as a Frenkel form for the γ-surface, but the relations may still be regarded as generic behavior of BCC crystals since real γ-surfaces should not deviate very far from the Frenkel form. More subtle material-dependent properties would require material-specific γ-surfaces. This has not been done so far for the kink-pair formation problem, but should be a straight-forward task to do.

### 3.1.3. Three-dimensional atomistic simulation of kink-pair activation

A rigorous atomistic treatment of activation should involve rate theory. One classical approach to calculate reaction rates is the transition state theory [67], and this involves calculating partition functions for both the reactant neighborhood and the saddle dividing surface. Mills et al. [68] have recently proposed that one can bypass calculating partition functions by calculating a reversible work
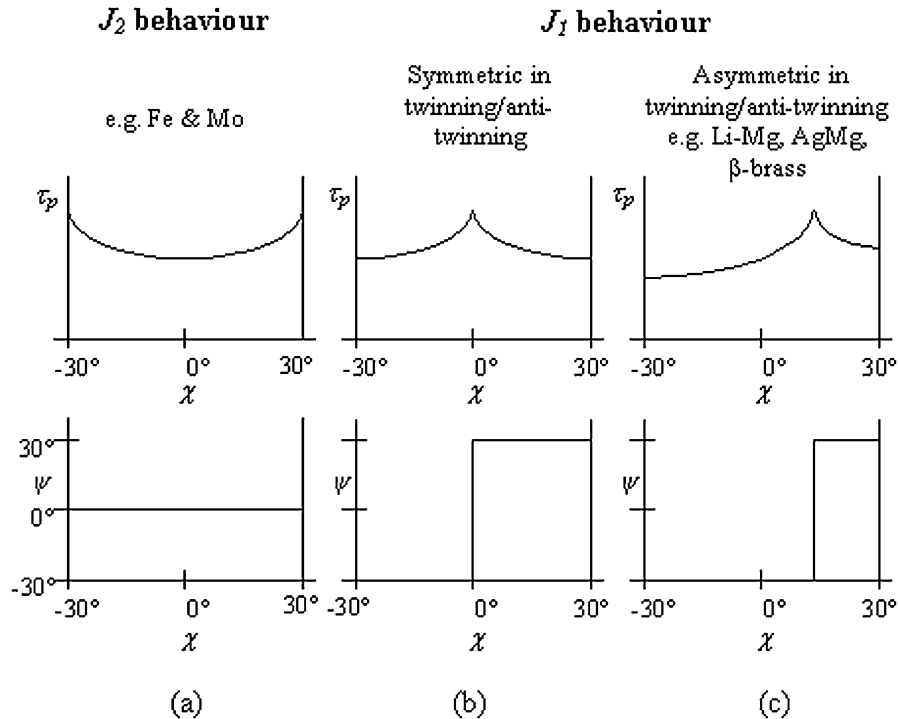
Fig. 8. Schematic Peierls stress ($\tau_p$) vs $\chi$ relations for $J_2$ and $J_1$ behaviour. $\chi$ is the orientation of the maximum resolved shear stress plane, measured from a {1 0 1} reference plane towards the direction of the anti-twinning {1 1 2} plane. $\psi$ is the orientation of the actual slip plane.
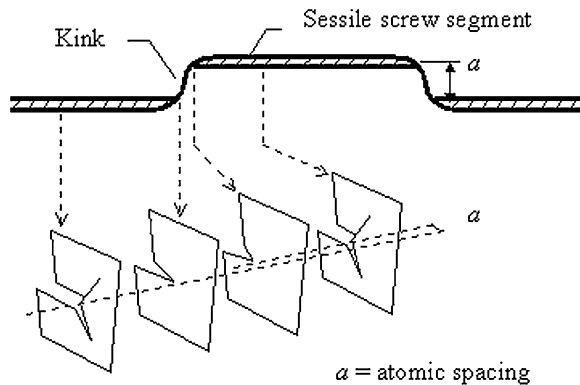


Fig. 9. Modeling kink-pair using a Peierls–Nabarro approach [59,60].

function instead. The new approach has still not been applied to calculating dislocation activation problems, presumably because the computing power to handle the entire phase domain on the reactant side of the saddle dividing surface is still too large for such problems. However, within the

harmonic approximation, the rate $\Gamma$ of a reaction can be simplified into $\Gamma = v^*\exp(-H/kT)$, where the activation energy $H$ is simply the energy difference between the saddle point and the ground state, and $v^*$ is an effective frequency equal to the ratio of products of the normal mode frequencies evaluated at the ground state and saddle point. Hence if the saddle point configuration can be located, $H$ can be evaluated. One way to locate the saddle point in an atomistic picture is to employ the so-called "nudged elastic band" method of Mills et al. [68]. This method assumes only knowledge of the reactant and product states. Equally spaced replicas of the system are then constructed along an initially chosen path joining these two states, as shown in Fig. 11. Each replica is then relaxed with respect to degrees of freedom which are perpendicular to the path. In this way, the minimum energy path (MEP) connecting the reactant and product states can be located, and the saddle point is simply the highest energy state on the MEP.
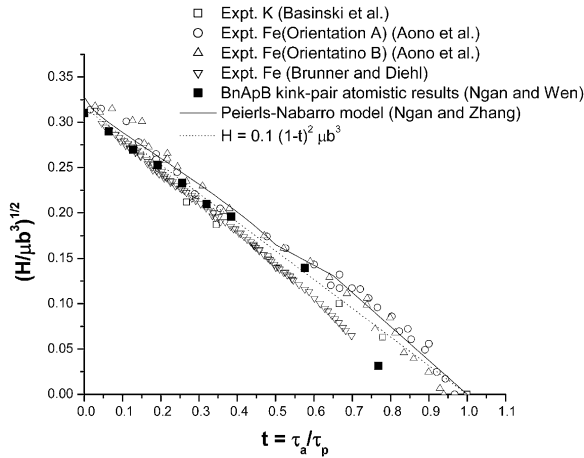
Fig. 10. Activation energy for slip (*H*) vs normalized stress $t = \tau_a / \tau_p$ in BCC metals. $\tau_a$ is applied shear stress, $\tau_p$ is Peierls stress at zero temperature. Data for potassium from Ref. [64], iron from Ref. [65,66]. For the iron data by Aono et al. [65], results at two stress orientations are shown: orientation A is close to the center of the unit triangle, and B is close to [101]. Also shown are the atomistic simulated activation energies for the lowest energy kink-pair (BnApB) using a BCC iron potential [63], as well as the prediction from a Peierls–Nabarro model [60].
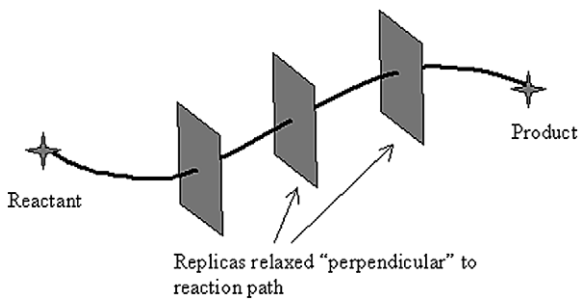


Fig. 11. Schematic illustrating the "nudged elastic band" method.

The nudged elastic band method (NEBM) was first applied by Rasmussen and co-workers [69,70] to investigate dislocations problems. They employed the NEBM to calculate the MEP for the Friedel–Escaig cross-slip mechanism in screw dislocations in copper. These authors found that the cross-slip behavior of screw dislocations in FCC metals exemplified by copper is by-and-large consistent with the classical predictions by Friedel and Escaig. However, in screw dislocations in BCC,

a few hitherto unknown results were revealed by simulations using the NEBM [61–63]. A major difference between a screw dislocation core in BCC and one in FCC is that the former, if threefold dissociated, is more complicated in that it exhibits degenerate configurations which are mirror images of one another. The degeneracy in BCC leads to a number of possible configurations of kink-pairs [71], as opposed to the only one form as in FCC in which the degeneracy does not exist. Fig. 12 shows the different kink configurations in BCC. These kink configurations can be denoted by a nomenclature scheme proposed by Duesbery [71], in which the two degenerate states of the screw core are labeled as "A" and "B", and the kinks are labeled as either "p" or "n" according to whether
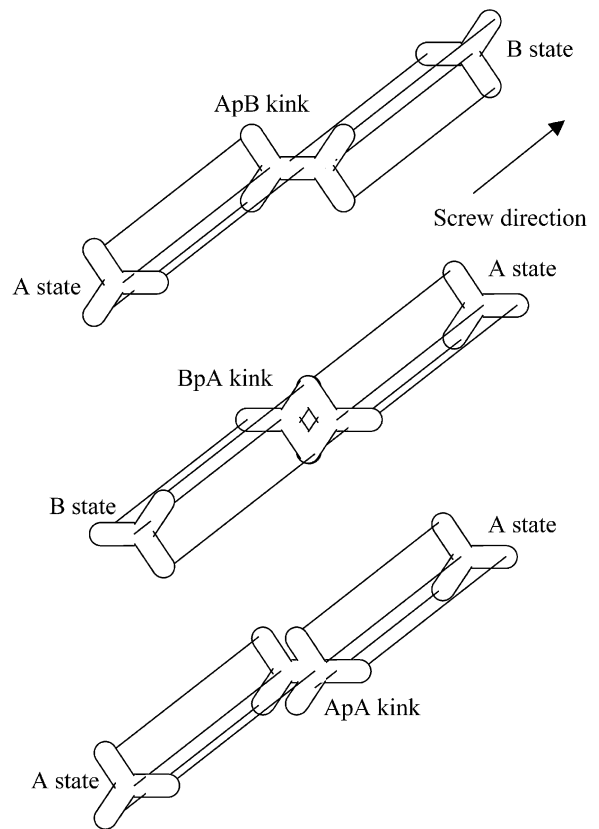


Fig. 12. Three-dimensional schematic illustrating different kink configurations in the BCC structure. The BpA kink is a high energy kink because the arms of the states of the screw dislocation intersect in the kink region.

they point along the positive or negative Peach–Koehler force direction, respectively. Because of configurational asymmetry, some of the kink configurations in Fig. 12 will have higher energies than others. A simple physical argument shows that kinks such as ApB and BnA are low energy configurations, because the "arms" of the dissociation of the A and B states on either side of the kinks are kept apart in the kink regions. (The ApB kink is in fact diad-related to the BnA kink and hence these are equivalent configurations, and so are AnB and BpA, AnA and BpB, and so on.) If the dissociation "arms" intersect in the kink region, as in configurations such as AnB and BpA, a higher energy can be expected because large distortions may be expected near the intersection locations. Simulations using the NEBM confirm these [63]. Fig. 13 shows the simulated activation energies of the different kink-pairs using an embedded atom potential suitable for BCC iron. Here, it can be seen that the BnApB kink-pair, comprising the low energy kinks BnA and ApB, has the lowest energy, while the AnBpA kink-pair, which comprises the high energy kinks AnB and BpA, has the highest energy. The kink-pairs comprising homogeneous kinks such as AnA, BpB, etc., have intermediate degrees of interaction at the kink regions, and hence their energies are intermediate as shown in Fig. 13.
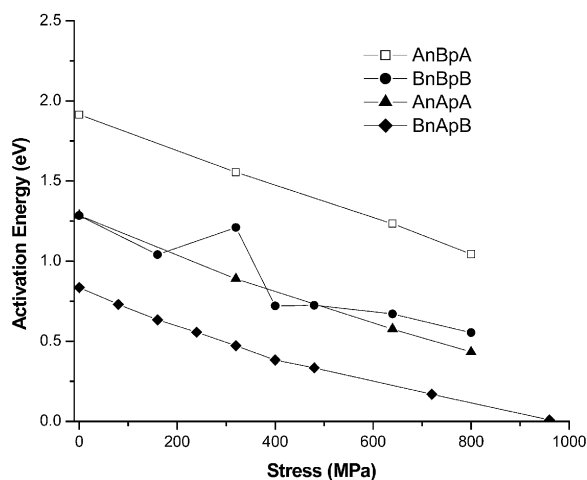


Fig. 13.   Simulated activation energies of different kink-pairs in BCC Fe [63].

The above asymmetries in kink energies have important implications in the glide process of an advancing screw dislocation in the BCC lattice. Suppose only the low energy ApBnA (or the equivalent BnApB) kink-pair can occur, a dislocation originally in the A state will jump to the B state on the next Peierls valley along the positive (say) Peach–Koehler force direction by the nucleation and expansion of the ApBnA kink-pair. However, the new B state cannot jump forward by another step to either the A state or the B state *on the same slip plane*, because the high energy BpAnB or BpBnB kink-pair, respectively, will have to be involved. To keep the energy low, the new B state will have to cross-slip by jumping to an A state on an inclining slip plane, and this process repeats itself [63]. The glide path will then have to be zig-zag on each atomic step. This explains the "pencil glide" phenomenon, or characteristic (ii) in Section 3.1.1. It should be noted that this new explanation of pencil glide hinges on the asymmetry of the kinks, and is therefore very different in spirit to the traditional explanation stemming from the observed behavior of straight dislocations under stress in 2-D atomistic simulations [48–50]. Since glide at finite temperatures ought to involve kink mechanisms, the present explanation should be more pertinent. The simulated energies of the BnApB kink-pair are also plotted in Fig. 10, and it can be seen that they agree reasonably well with the experimental results and the Peierls–Nabarro relation in Eq. (3.3).

## 3.2. Kear–Wilsdorf lock formation in the $L1_2$ superlattice

Another prominent group of materials in which 3-D activation processes of dislocations are important are $L1_2$ intermetallics which exhibit a flow stress anomaly. Based on atomistic results on straight $1/2\langle 1\,1\,0\rangle$ superpartial dislocations, Paidar, Pope and Vitek (PPV) proposed that the strength anomaly is due to the thermally activated formation of incomplete Kear–Wilsdorf locks (or later known as "PPV" locks) for screw superdislocations [72]. As illustrated in Fig. 14, a PPV lock is formed by either a one-step jump by $b/2$ or a two-step jump by $b$ of the leading superpartial from
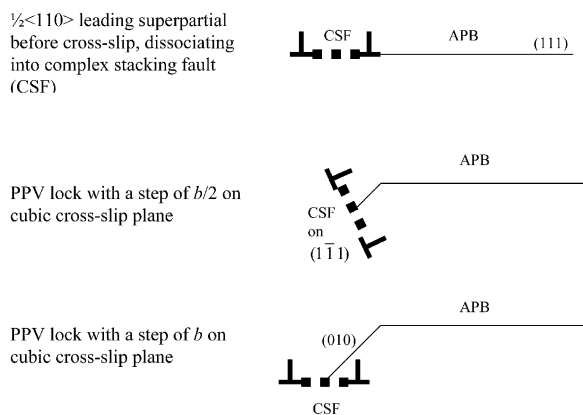
½<110> leading superpartial before cross-slip, dissociating into complex stacking fault (CSF)

PPV lock with a step of *b*/2 on cubic cross-slip plane

PPV lock with a step of *b* on cubic cross-slip plane



Fig. 14.   Two forms of PPV locks.

an original (1 1 1) plane onto a (0 1 0) cross-slip plane, where *b* is the Burgers vector of the $1/2<1 1 0>$ superpartial dislocation. Hirsch [73] proposed a detailed theory of the flow stress anomaly, which is based on the PPV locks but has detailed elaboration on the subsequent dislocation development after a two-step PPV jump of the leading superpartial to form a strong lock, as well as on the unzipping process of such a lock which is predicted to give rise to the nearly zero strain-rate sensitivity of the flow stress. In Hirsch's theory, the apparent activation energy is identical to that in the PPV model, namely, the activation energy for cross-slip from a primary (1 1 1) slip plane onto a (0 1 0) plane by one atomic step in a kink-pair model. Hence, the PPV lock formation is the rate-controlling process in Hirsch's theory.

The stability of the PPV locks, however, remains controversial. Schoeck [74] has predicted that the one-step PPV lock produced by a (*b*/2) jump is energetically unstable with respect to the planar state on the (1 1 1) plane before the jump. Schoeck's treatment is a planar Peierls–Nabarro model. Three-dimensional atomistic simulations on the dislocation processes in intermetallics are rare, and the only study to-date is that by Parthasarathy and Dimiduk [75], who have studied the structures and energies of the PPV locks and the jogs at the intersection between a locked and an unlocked segment.

The NEBM should be a convenient method to investigate the process of PPV lock formation. An active project is underway along this direction, and in what follows, some results are presented to provide a snapshot of the current activities. The main aim of these simulations is to elucidate the relative importance of antiphase boundary (APB) energy anisotropy, Yoo's torque [76] and Escaig effect in controlling the formulation of PPV locks.

### 3.2.1. Simulation method

The simulations below employed the embedded atom potential for Ni₃Al developed by Voter and Chen [77]. The same potential was used by Parthasarathy and Dimiduk [75], so that direct comparison can be made with that study. The full superdislocation has a dissociation width of larger than 6 nm and hence to speed up calculations, only the leading superpartial was included in the simulation block. The effect of the trailing partial was incorporated through applying the corresponding anisotropic elasticity Volterra field to the boundary region of the simulation block. The simulation cell was a rectangular block with a length of ~10 nm along the <1 1 0> screw direction, and a dimension of ~5 nm in the other two orthogonal directions which were along a <1 1 1> and <1 1 2> direction, respectively. The trailing APB was placed on the (1 1 1) plane parallel to one edge of the simulation cell. To implement the NEBM, 18 equidistant replicas were set up between the reactant and product states (see Fig. 11). The calculations were parallelized using typically six processors, each handling three replicas. If a stable intermediate state was found, the calculation was repeated by breaking the reaction into two steps, the first from the reactant state to the intermediate state, and the second from the intermediate state to the product state. Constrained relaxation was carried out until there was no noticeable change in the energy along the MEP, and typically this corresponded to an average residual force perpendicular to the MEP of the order of $10^{-4}$ eV/Å.

The PBC was applied along the <1 1 0> screw direction. In the $L1_2$ close-packed structure, free boundaries cannot be used for the other two directions because the Peierls stress is too small, and hence the simulated dislocation would be easily attracted to a free surface. Instead, flexible boundaries updated using a lattice Green's function were

used [78]. The net energy change during the dislocation motion is the configurational energy minus the work done by the applied stress field and the stress field due to the trailing superpartial dislocation, plus the long-range strain energy developed during the kinking process. The work done due to the applied stress can be calculated by determining the average force acting on the atoms on the interface between the atomistic and the outer Green's function region due to the applied stress, and multiplying this by the displacement of these atoms during the core change. The work done due to the trailing superpartial, i.e. the well-known Yoo's torque effect [76], is likewise calculated as the product of the force due to the Volterra field of the superpartial on the atoms lying on the interface between these regions, and the movement of these atoms during core changes. The strain energy in the continuum region due to core changes is calculated by the following formula:

$$\text{energy} = \frac{1}{2}\oint\sum_{ij}\sigma_{ij}u_i\mathrm{d}s_j, \tag{3.4}$$

$$\sigma_{ij} = \frac{1}{2}c_{ijkl}(u_{k,l} + u_{l,k})$$

where the integration is over the interface between regions 2 and 3; $\mathrm{d}s_j$ is an element of the interface with normal pointing towards the center of the simulation block, and $c_{ijkl}$ are the elastic constants. $u_i$ here is the displacement with respect to the reactant state of a finite element of volume containing $\mathrm{d}s_j$. The displacement $u_i$ is calculated as the average displacement difference between a particular state along the MEP and the reactant state of all the atoms situated inside the element containing $\mathrm{d}s_j$.

### 3.2.2. Simulated minimum energy paths for PPV lock formation

While details will be published separately, a few key results will be outlined here to provide a perspective. In the results below, the reactant state was a 1/2<1 1 0> leading superpartial spreading on the primary (1 1 1) plane (top diagram in Fig. 14), and the product state was a two-step PPV lock in which the same superpartial had cross-slipped onto the (0 1 0) plane by $b$ and had spread on a (1 1 1) plane parallel to the original slip plane (bottom dia-

gram in Fig. 14). The MEP was automatically located by the NEBM.

*3.2.2.1. Effect of Escaig stress*    Fig. 15 shows the simulated MEPs at different stress states. It can be seen that in the absence of an Escaig stress, which is a stress along the edge direction on the primary slip plane, the MEP exhibits a high activation energy of 4.0 eV at a stress of 160 MPa on the (0 1 0) cross-slip plane. This energy is somewhat lower but comparable to the results obtained by Parthasarathy and Dimiduk [75], who have used the same potential but a very different constraining method to simulate the unstable kink-shape, and have concluded an activation energy for the same PPV jump to decrease from ~4.9 to ~4.2 eV when the stress is increased from 0 to 500 MPa on (0 1 0). Such activation energies are obviously too high compared with the experimentally determined apparent activation energy for the flow stress anomaly in Ni$_3$Al, which should yield a locking activation energy in the range of 0.5–0.9 eV [75].

In the absence of an Escaig stress, the present simulation results show that the PPV jump by $b$
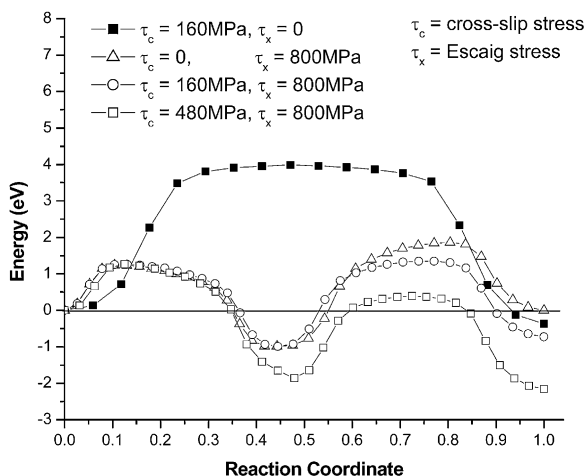


Fig. 15.    Effects of cross-slip stress and Escaig stress on minimum energy path (MEP) of PPV lock formation. The reaction state (reaction coordinate = 0) corresponds to planar dissociation on primary octahedral plane before cross-slip. The product state (reaction coordinate = 1) corresponds to the PPV jump by 1$b$ on the cross-slip cube plane. In some MEPs, an intermediate state occurs and this corresponds to the PPV jump by $b$/2 on the cross-slip cube plane.

does not involve the $b/2$ PPV jump (middle diagram in Fig. 14) as an intermediate step. Parthasarathy and Dimiduk concluded that the $b/2$ PPV jump is unstable unless under an exceptionally large cross-slip stress exceeding 700 MPa. However, the present simulation indicates that the $b/2$-jump can be stabilised by a large enough Escaig stress as well. The results in Fig. 15 show that under a high Escaig stress of 800 MPa on the primary (1 1 1) plane, the $b$-jump indeed involves an intermediate state which was found to be the $b/2$-PPV lock. The intermediate state of the $b/2$-PPV lock occurs only when the Escaig stress is higher than ~500 MPa. Below this stress value, the $b$-jump remains as a single process with an activation energy above 4 eV. The high Escaig stress required here may not be realistic because the Voter and Chen potential applied here predicts a too small value for the complex stacking fault energy. Therefore, in reality, the spreading of the $1/2 < 1 1 0 >$ superpartial on the primary octahedral plane may be narrower than in the simulations using this potential. In any case, the occurrence of $b/2$-PPV lock as an intermediate state for the $b$-jump drastically reduces the activation energy to only slightly above 1 eV as shown in Fig. 15. The discrepancy with the experimental value of 0.5–0.9 eV is therefore smaller. The reason for the drastic reduction of the activation energy with the intermediate state is similar to the situation depicted in Fig. 12 for the BCC screw core, namely that the $b/2$-PPV lock dissociates on a plane inclined to the original slip plane as Fig. 14 shows, while the $b$-PPV lock dissociates on a plane parallel to the original slip plane. The strain in the kink regions in the critical kink-pair configuration corresponding to the formation of the $b/2$-PPV lock is therefore more distributed, resulting in a lower energy. Another observation from the results in Fig. 15 is that the activation energy from the reactant to the intermediate state (~1.2 eV) is independent of the cross-slip stress. The reason is that the center of the leading partial roughly remains on the same (1 1 1) plane during this process, and hence the cross-slip stress can do little work in this process. The second stage from the intermediate state to the product state, however, has an activation energy depending weakly on the cross-slip stress.

### 3.2.2.2. Effect of the Yoo torque vs APB energy anisotropy

Yoo [76] proposed that in an elastically anisotropic material, the trailing superpartial exerts a torque on the leading superpartial in the cross-slip direction. To elucidate the relative importance of the Yoo-torque and APB energy isotropy between (1 1 1) plane and (0 1 0) plane in the driving force for cross-slip, another simulation was conducted in which the trailing partial was placed infinitely far away. This has the effect of switching off the Yoo-torque, while retaining the APB anisotropy effect. The simulated MEP is shown in Fig. 16 as the solid symbols. Here, the cross-slip stress is turned off to reveal the pure effect of APB anisotropy, but a large Escaig stress is applied to result in the intermediate state. The MEP exhibits an energy gain of 0.197 eV/$b$ after the PPV jump by $1b$ on the (0 1 0) plane. This is due to the creation of an APB ribbon of $1b$ wide on the (0 1 0) plane after cross-slip. This energy gain converts to an energy of 494 mJ m$^{-2}$ for the APB strip on the (0 1 0) plane, which is significantly higher than the 83 mJ m$^{-2}$ for an infinitely wide APB on (0 1 0) calculated by the same potential. The much higher energy of the APB strip on (0 1 0) in the PPV lock is thought to be due to the constraining effects imposed by the bounding superpartial [79] and the "corner" effects at the intersection between the APBs on the (0 1 0) and (1 1 1) planes [80]. Since
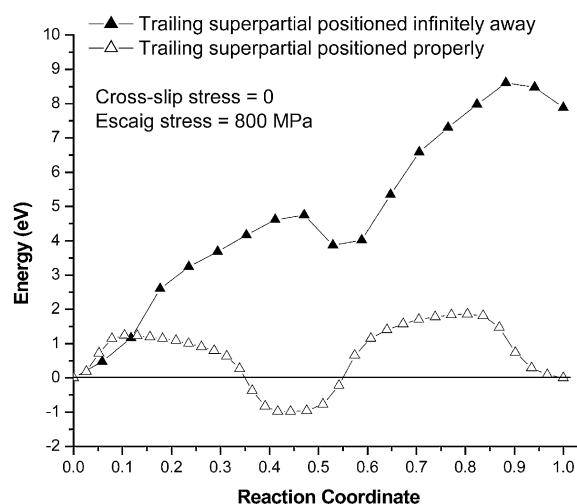


Fig. 16. Effect of switching off Yoo's torque on MEP of PPV lock formation.

the APB energy on (1 1 1) is only about 142 mJ m$^{-2}$, the APB energy anisotropy alone offers no and indeed a negative driving force for the PPV lock formation. The constraining effects on the narrow strip of the APB on the cross-slip plane of a PPV lock thus appears to be an important factor in the consideration of the driving force for the formation of such a lock.

The effect of the Yoo-torque on the driving force for cross-slip can be seen by comparing the MEP without the trailing superpartial and that with the trailing superpartial properly positioned in Fig. 16. In the MEP with the trailing superpartial properly positioned, the product state (the b-PPV lock) has fortuitously similar energy as the reactant state, but in the simulation, the trailing superpartial was held fixed. In reality, the trailing superpartial should have come forward to shorten the APB on the primary (1 1 1) plane during the cross-slip of the leading superpartial, and thus, with the presence of the Yoo-torque, the whole cross-slip process should have a positive driving force. The results in Fig. 15 indeed show that an increasing stress on the cross-slip plane would also lead to an increasing driving force for cross-slip as expected. Work is underway to automatically reposition the trailing superpartial during NEBM relaxation to more realistically simulate the MEP during PPV lock formation.

### 3.3. Dislocation interaction with other lattice defects

An area where atomistic modeling will play a particularly important role in the future is the interaction of dislocations with other lattice defects. In experiments, these processes usually cannot be observed individually, but they clearly control plasticity over a wide range of loading conditions. The lattice defects of interest range from individual point defects and clusters of them to other dislocations, surfaces, interfaces and second phase particles.

Dislocation point defect interaction is of course the key to climb processes and high temperature deformation. At reasonably low temperatures they account for solid solution hardening or the dependence of the flow stress of intermetallic alloys on

composition [81]. These effects can now be studied reasonably well that systematic investigations have now begun. An example is B2 NiAl, where dislocation interactions with vacancies and antisite defects have been investigated [81]. They tend to give values which are in reasonable account with experiments on off-stoichiometric alloys and even explain flow stresses of stoichiometric NiAl at intermediate temperatures [82]. However, quantitative comparison to the experiment requires dedicated multiscale approaches which still need to be developed further.

Dislocation dislocation interaction is the prime domain of current multiscale modeling efforts [83]. Atomistic simulations sometimes show unexpected reaction products [84] but most often the detailed core effects need not be considered and the modeling can safely be done on a discrete dislocation level which is based on the elastic interactions between dislocations [18–21]. This, in short, can be regarded as the main outcome of several recent atomistic simulations of dislocation intersection and junction formation and their very elegant comparison to dislocation modeling [85–87]. Nevertheless, these studies have also shown the important role atomistic modeling can provide in assessing assertions from coarser simulations on a more fundamental basis. In some cases, the atomistic modeling may then be used to determine the relevant parameters for the coarser models.

Of genuinely exploratory nature and not specifically guided by detailed experimental investigations (for experiments on a model system of bubble rafts with grain boundaries, see [88]) are current studies of the deformation of nanocrystalline materials. Following the established understanding of the effect of dislocation interaction with grain boundaries, one expects metals to become increasingly harder as their grain size is reduced (see [89] for an excellent review of size effects in materials). The Hall–Petch effect is expected to lead to a scaling of flow stress with the inverse square root of grain size. Nanocrystalline metals are therefore expected to exhibit fantastic hardness. Experimentally they do not quite reach such hardness and furthermore the hardness may even show direct scaling with grain size. Diffusion processes are held responsible for this behavior

[89] but atomistic simulations of such nanocrystalline aggregates have also shown grain boundary sliding to be important [90,91]. With the ability to handle increasingly larger grain structures, the simulations of nanocrystalline metals now just hit the size scale where dislocation processes begin to contribute again [92–94]. Dislocation nucleation from the grain boundaries is one of the processes which current investigations are focusing on. In principle, sufficiently large atomistic systems can now be handled to give the transition to the classical Hall–Petch behavior. Such studies are expected soon and will then provide the starting point for more systematic investigations of the interplay between grain boundaries and dislocations.

One of the key processes in this scenario, dislocation nucleation, is also studied by MD simulations of a running crack in a three-dimensional notched solid [95]. A Lennard–Jones crystal, loaded in tension in a <1 1 0> direction, first shows brittle crack propagation and then develops a crack tip instability, which results in the massive generation of dislocations at the crack tip. The simulations clearly show that non-blunting dislocations on inclined glide planes play a very important role in the plastic zone which is developing around the crack tip. Fig. 17 displays the crack at the point of instability and the development of the plastic zone. Unfortunately, such studies are still too demanding to systematically study imperfections in the crack front and other possible causes for dislocation nucleation.

## 4. Brittle fracture processes

Fracture is a phenomenon which spans many different length scales. The macroscopic dimensions of the crack and the specimen determine the intensity of the stress concentration at the crack tip and are equally important as the microstructure of the material, which provides preferred fracture paths. Ultimately, fracture reduces to the breaking of atomic bonds, which in the case of brittle fracture occurs at an atomically sharp crack tip [96,97]. In a perfectly brittle material, the crack moves by no other process than the breaking of individual bonds between atoms. Nevertheless, traditional theory of brittle fracture processes does not focus on individual atomic bonds but resorts to the treatment of Griffith [98], which is based on continuum thermodynamics. Following Griffith, one may regard the static crack as a reversible thermodynamic system for which one seeks equilibrium. The equilibrium condition leads to the so-called Griffith criterion, which balances the crack driving force and the material resistance against fracture. With the implication of thermodynamic equilibrium, Griffith's picture provides a reference value for the analysis of the crack driving forces. It however cannot explain why and how fracture proceeds. From an atomistic point of view, one immediately identifies materials resistance against fracture with the forces needed to break the crack tip bonds successively. The first atomistic studies of fracture [99] showed that the discrete bond breaking event manifests itself in a finite stability range, which was attributed to the discreteness of the lattice and called the "lattice-trapping" effect. Lattice trapping causes the crack to remain stable and not to advance/heal until loads $K^{+,-}$ somewhat larger/smaller than the Griffith load are reached. Other influences of the atomic nature of a crack have recently been summarized in a series of articles in the *MRS Bulletin* [100]. Consequences of the lattice trapping have been reviewed [101,102] and only one particularly important aspect of the lattice trapping, crack propagation anisotropy, is discussed below.

### 4.1. Lattice trapping and the cleavage anisotropy in silicon

Silicon is reported to have two principal cleavage planes: {1 1 1} planes, usually the easy cleavage planes, and {1 1 0} planes [103,104], the planes of easy cleavage in polar III–V semiconductors. The most accurate constant-$K$ experiments [103] seem to show that {1 1 0} planes have a slightly lower fracture toughness than {1 1 1} planes. For both cleavage planes, the measured fracture toughness gives surface energies ($\gamma_{1\,1\,0}$~2.3 J/m$^2$, $\gamma_{1\,1\,1}$~2.7 J/m$^2$) which are significantly larger than the values calculated atomistically using density functional theory (DFT)-based quantum mech-
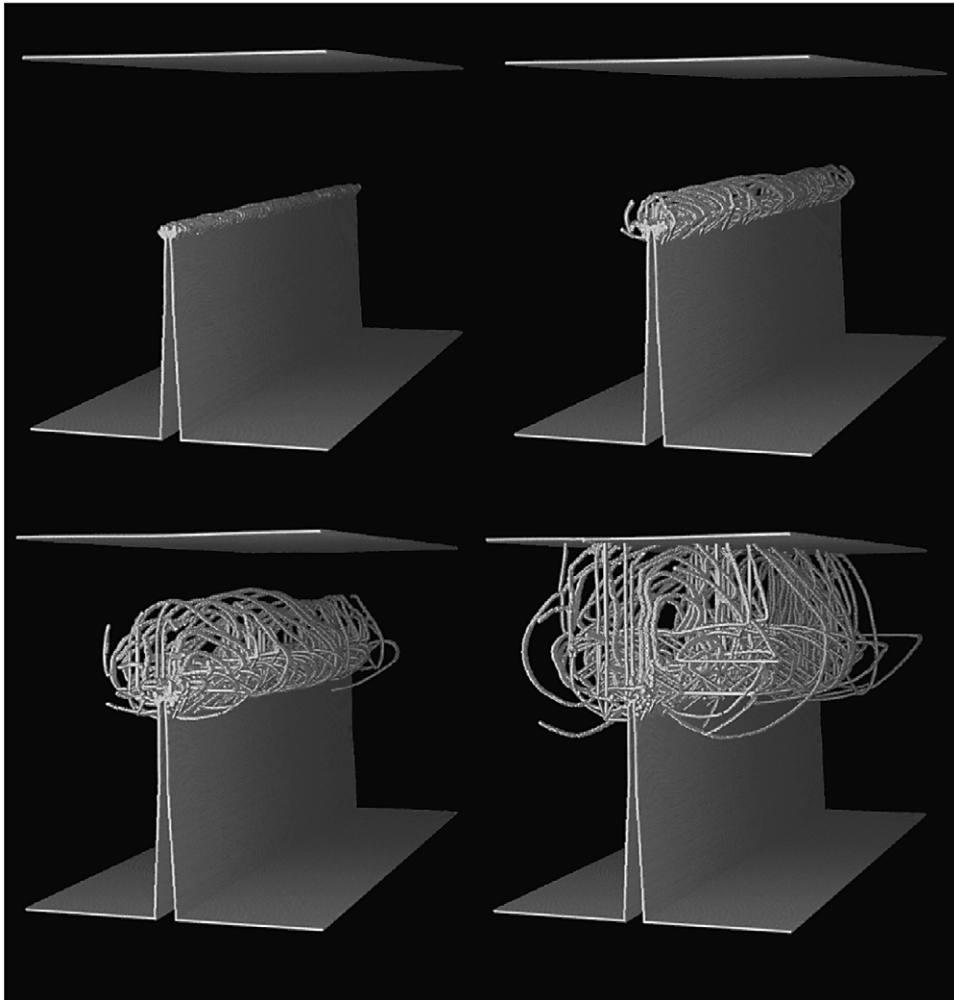
Fig. 17. Three-dimensional MD simulation of crack propagation and dislocation generation in an FCC crystal. Atoms are shown only if their energy exceeds a critical value. This value is chosen to select only the atoms at crystal lattice defects and surfaces. The four frames display the crack after some brittle crack propagation at the point of instability to dislocation emission (upper left) and the further development of the plastic zone around the crack tip. (Courtesy of F. Abraham.)

anical methods ($\gamma_{1\,1\,0} \sim 1.7$ J/m², $\gamma_{1\,1\,1} \sim 1.4$ J/m²) [105].

Propagation direction anisotropy has been observed for both cleavage planes. The preferred propagation direction is along $<1\,1\,0>$ on both cleavage planes [103,104]. On the {1 1 1} fracture surface, the anisotropy with respect to propagation direction is minimal. In contrast, cleavage on the {1 1 0} plane is extremely anisotropic. Propagation along the $<1\,1\,0>$ direction results in nearly perfectly flat fracture surfaces [103,104]. Attempts to

achieve propagation in the $<0\,0\,1>$ direction, perpendicular to the preferred direction, have not been successful because the crack deflects onto {1 1 1} planes [104,106]. The relation of the calculated surface energies and elastic anisotropy cannot account for this deviation of the crack [107] and an atomistic investigation therefore is attractive.

Based on ab initio calculations of the crack tip stability, the anisotropy in fracture behavior with respect to the propagation direction on the {1 1 0} plane was recently explained as a consequence of

a difference in lattice trapping for the different propagation directions [107]. A {1 1 0} crack propagating in the "easy" <1 1 0> direction (Fig. 18(b)) continuously opens successive bonds at the tip of the crack. This continuous process leads to a relatively small trapping, and it can be argued that the trapping may further decrease as the size of the model (specimen) is increased. In contrast, a crack driven in the "difficult" <0 0 1> direction on the {1 1 0} plane, displayed in Fig. 18(a), shows

a clearly discontinuous bond breaking. Fig. 18(c) shows the bond distances of the crack tip bonds (labeled "B" in Fig. 18(a) and (b)) for both systems. Further analysis of this discontinuous bond breaking process shows that it is mainly a result of the relaxation of the six or eight atoms around the crack tip and connected with a significant load sharing between the crack tip bond and the one above [105]. Comparing both the loading and unloading processes, it is seen that the discontinu-
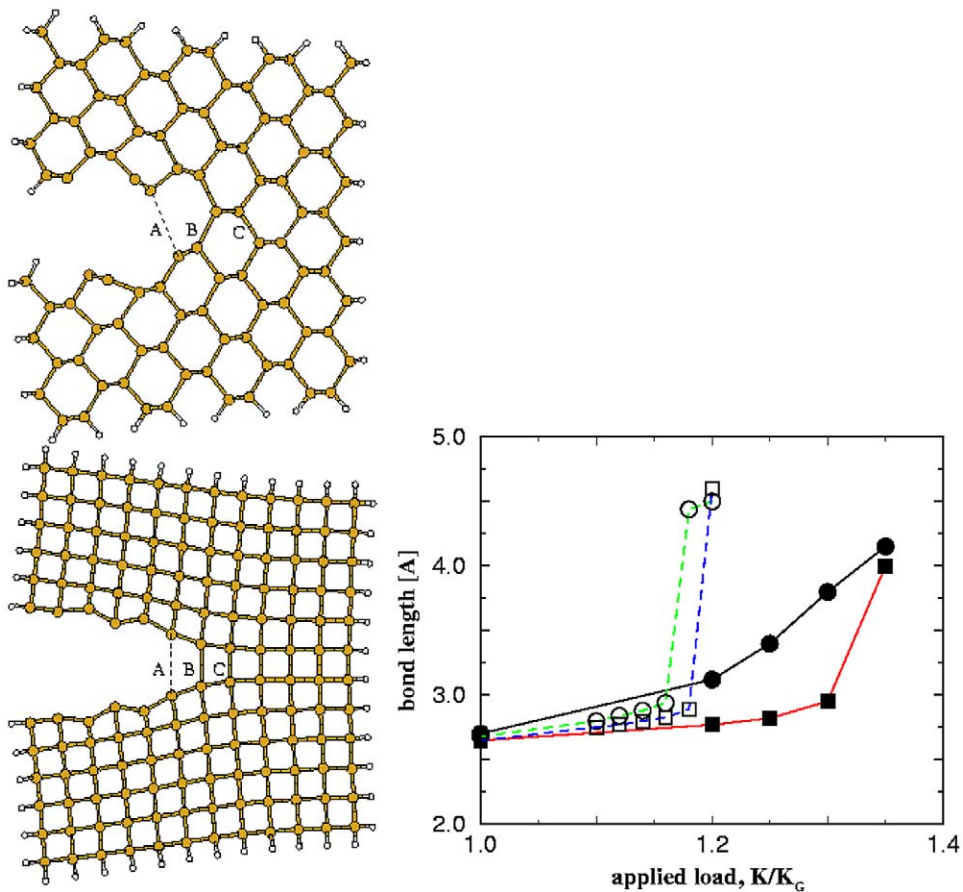


Fig. 18. Relaxed atomic configurations (using ab initio methods) of (top) the silicon {1 1 0}<1 1 0> crack, which is propagating in a <0 0 1> direction, and (bottom) {1 1 0}<0 0 1> crack, propagating in the <1 1 0> direction. The outermost two layers of silicon atoms are held at the positions given by the linear elastic solution for the displacement field of the crack (for a load of $1.2K_G$). Their dangling bonds are saturated with hydrogen atoms. The bond distance for the bonds labeled B is displayed (filled symbols) as a function of the applied load in the diagram on the right. While the {1 1 0}<0 0 1> crack (circles) shows a continuous increase in bond length, a discontinuous bond breaking at an applied load of $1.35K_G$ is found for the {1 1 0}<1 1 0> (squares) crack. The open symbols are for a modified Tersoff potential, which does not well reproduce the bond breaking characteristics of the ab initio calculations [102].

ous bond breaking is also connected with a larger lattice trapping range [107]. This difference in the trapping effectively destabilizes the {1 1 0} crack propagation in the <0 0 1> direction against deflection onto an inclined {1 1 1} cleavage plane. Thereby lattice trapping appears to provide the only reasonable explanation for the experimentally observed cleavage anisotropy with respect to the propagation direction for the {1 1 0} cracks in silicon.

## 4.2. Dynamics of brittle crack propagation

The fracture of materials can be a dynamic process, at least in the final stage of supercritical propagation. Although this last stage of fracture might at first seem almost irrelevant, closer consideration shows that it is precisely the dynamics of the brittle crack which competes with the rate-dependent plasticity in the near tip region to determine whether a propagating crack can ever be stopped. The dynamic crack propagation has therefore recently attained much attention.

The first set of atomistic investigations of dynamically moving cracks were directed towards understanding the steady-state propagation, crack speed and the onset of dynamic instabilities. Analytical atomistic studies [108] on simplified one- and two-dimensional structures show that the dynamically propagating crack can only access a limited velocity regime. After initiation, crack tip speed immediately reaches about 20% of the Rayleigh wave velocity and approaches a branching instability at about half the Rayleigh wave velocity [108]. The instability manifests itself in the breaking of bonds at the flanks of the crack before the breaking of the next bond in propagation direction and is interpreted as a branching instability.

MD simulations [109] of the propagation of a mode I crack with a straight crack front and a short periodic length along the crack front (quasi-two-dimensional geometry) essentially confirm the analytic results. They confirm a lower band of forbidden velocities for the straight crack and also reveal an upper critical velocity. The upper critical velocity for the mode I crack is shown to strongly depend on the non-linearity of the atomic interaction. For harmonic snapping spring force laws [109] and for open crystal structures with strong

directional bonds [110,111] the velocities can be almost as high as the Rayleigh wave velocity, the relativistic upper limit. Only 40% of the Rayleigh wave velocity is reached for close-packed crystals and more realistic non-linear atomic interactions [109]. Up to 50% of the shear wave speed is reached in the more complex quasicrystalline structures [112]. Increasing temperature reduces this band of forbidden velocities and successively allows cracks to also propagate at lower speeds [113,114]. In amorphous or quasicrystalline structures, increasing temperature may also lead to a change in crack propagation mechanism from the propagation of a distinct crack tip to crack propagation by successive opening of pores or daughter cracks in front of the main crack and their backward propagation (see Fig. 19) [114–116]. This of course drastically reduces the crack propagation speed.

Above the critical velocity, the MD simulations reveal a rich set of different types of instabilities depending on the crystallographic orientation of the crack and on the crystal structure [109,110,112]. The generation of cleavage steps and dislocation emission are usually observed at lower overloads, while crack bifurcation was only observed at the highest overloads. Dislocation emission usually leads to a pronounced change in crack propagation direction.

Large scale MD simulations have recently confirmed continuum mechanical analysis [117] on the fact that mode II cracks just like edge dislocations [118] are not bound by the shear wave speed as an upper limit [119]. They show a transition to intersonic propagation via the nucleation of a daughter crack out of a subsonic mother crack.

## 4.3. Brittle–ductile transition

The brittle–ductile transition commonly observed in BCC metals, i.e. point (vi) in Section 3.1.1, has often been linked to the low mobility of screw dislocations in the BCC lattice. However, a more complete analysis must involve mesoscale considerations, taking into account the mutual interaction amongst dislocations whose individual behavior, however, is governed by the physics of the dislocation core. Originally, the ease with
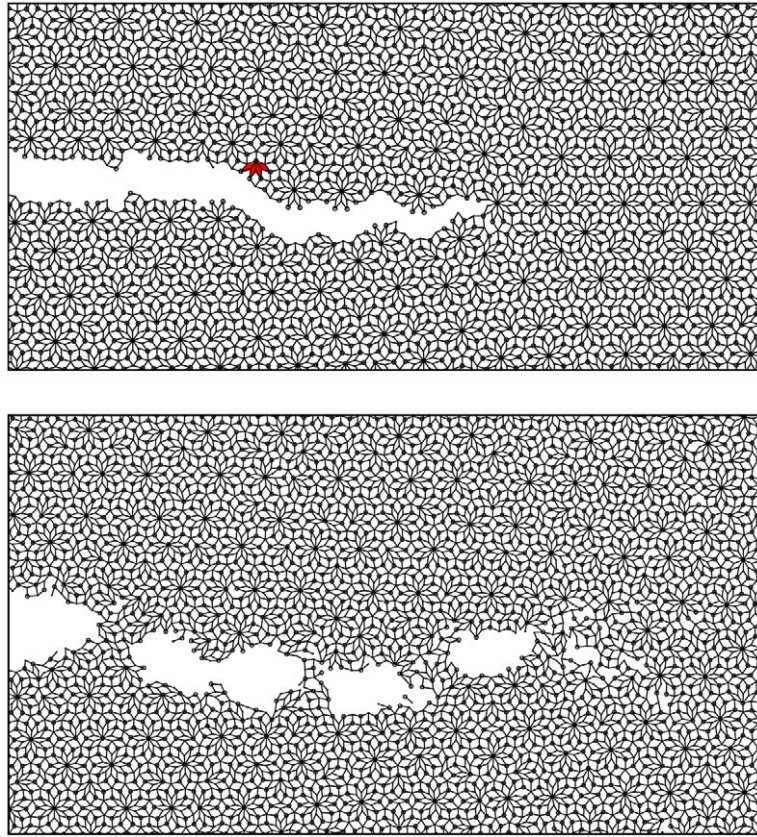
Fig. 19.   Crack propagation in a quasicrystalline structure: at low temperature ($0.1T_{melt}$, upper frame), the crack avoids strongly bound obstacles whenever possible but propagates essentially as a brittle crack. The crack propagation process and particularly the surmounting of obstacles is sometimes mediated by virtual dislocation emission [112]. Crack propagation speed reaches 50% of the shear wave velocity. At higher temperatures ($0.75T_{melt}$, lower frame), the crack propagation mechanism changes to nucleation, growth and coalescence of microvoids in front of the crack tip [114]. The crack propagation speed is then reduced to roughly 3% of the shear wave speed.

which dislocations can be emitted from sources in the vicinity of the crack tip or directly from the crack tip itself has been proposed to be a criterion for the BDT [120–122]. Ngan and Zhang [123] have recently extended these studies to include the non-planar dissociation of a screw dislocation ahead of a crack tip, and have shown that the presence of the crack as a free surface largely reduces the elastic resistance to a core transformation from a non-planar state to a mobile, planar state. Hence, mobility should not pose any problem for crack tip emission in the BCC structure. This conclusion was further supported by atomistic results [124]. Despite this, increasing experimental evidence

[125,126] seems to indicate that the BDT in BCC metals is controlled by the mobility of dislocations away from the crack tip. One distinguishing difference between BCC metals and covalent solids such as Si in terms of the BDT is that the activation energy of the BDT in BCC metals is in general much lower (by an order of magnitude) than the activation energy of bulk slip [125,127,128], while for covalent solids, the BDT activation energy is comparable to activation energy of bulk slip [129,130]. The much lower BDT activation energy in BCC metals could be interpreted in terms of the strong stress-dependence of the activation energy of slip, as expressed, for example, by Eq. (3.3), in

the vicinity of the highly stressed crack tip. However, recent discrete dislocation dynamics simulation [131] has shown that the effective activation energy of crack tip plasticity—even with stress-dependent activation energy—is only marginally reduced from the activation energy of bulk slip. This must be interpreted to clearly rule out the mobility of screw dislocations as the only decisive factor and the rate limiting step for crack tip plasticity and the BDT. It rather suggests that other factors such as the blunting edge dislocations [128,131], or the crack tip enhancement of the dislocation emission process itself [123,124], may play an important role. However, there remain many unknown facts amongst which the role of the initial dislocation density of the material and the nature of the dislocation sources near the crack tip are the most-needed ones. More experiments, dislocation dynamics simulations [18–21], and in particular more specific atomistic simulations are required to clarify these questions.

## 5. Outlook

Some of the most promising developments in the recent past are the fantastic improvements in the development of physically more transparent, environmentally dependent quantum mechanically based methods to describe the interatomic interactions. Most of these developments are based on tight-binding methods which are modified to allow for order-$N$ scaling behavior [132,133]. These models have first been developed for semiconductors (see [134] for a comparative assessment). The need for such methods for a reliable description of transition metals and intermetallics, however, is even greater [135] but this requires further improvements to account for the environmental dependence. Such improved descriptions are now gradually appearing [136–139]. They hold great promise to further lead atomistic modeling of materials properties away from generic, possibly crystal structure-specific to material-specific quantitative studies of dislocations, interfaces and fracture processes. Furthermore, such improved interaction models now open atomistic modeling of dislocations to new classes of materials which have

hitherto been out of the scope of classical atomistic simulation, like Laves phases or multicomponent alloy systems.

Another development which leads in the same direction but which has the capability to fully include first-principles accuracy in some part of the model are hybrid computational schemes which couple different levels of physics in one program. Forerunners of these developments have been the continuum–atomistic schemes and quasicontinuum approaches [140–142]. Recently, these have been extended to include quantum mechanical parts [55,143,144] or even to re-evaluate simple models of the atomic interaction during simulation, termed fitting on the fly [145,146].

Such quantum mechanics-based methods will be important for studies of the cleavage fracture and the general fracture behavior of more complex III/V or II/VI semiconductor crystals and of interfacial fracture. They may also be useful here for developing continuum models which can predict fracture. While the Peierls model for the dislocation allows quantum mechanical information to be included in semi-continuum studies of dislocation cores, no similarly powerful model exists for fracture and currently we have no predictive capability to determine the cleavage planes of a given brittle material other than full atomistic simulation. This certainly is a subject well worth further study and atomistic simulation.

The quantum mechanical accuracy will however be most urgently needed for the study of chemical attack at the crack tip. Although being of outstanding importance for the assessment of long-term behavior of ceramics, the effects of chemical reactivity at the crack tip as the origin of slow crack growth have not been sufficiently well understood so far. The simplest case is probably the well-known effect of moisture on the crack growth velocity in $SiO_2$ glass [96]. Such studies would not only be welcome by the glass community, but also would be urgently needed to better understand wafer bonding processes and the subsequent mechanical and thermal stability of wafer bonds [147]. Bonded silicon wafers develop thin $SiO_2$ interlayers in between which must be fractured again if the wafers shall be separated. Experiments show that a small amount of water enhances crack propa-

gation speed significantly, which suggest that the chemical attack of the stressed siloxane (Si–O–Si) bond by water is the key process [148].

Another area where we will certainly see increasing activity is the study of crack nucleation. Our understanding of crack nucleation processes is still at a very rudimentary level, but crack nucleation as the strength-determining factor is becoming increasingly common. The simplest and experimentally well characterized case is the crack nucleation at well defined wedge type notches in silicon [149]. Such notches often occur in microelectronic and micromechanical devices (MEMS) as a result of anisotropic etching. They are almost atomically sharp therefore lending themselves well for such studies. Similarly, crack nucleation from dynamically loaded silicon free surfaces [150], from grain boundaries or dislocations impinging on grain boundaries, will come into the focus of atomistic modeling. Similarly, for the dynamic fracture issues, nice and detailed experiments are available on silicon single crystals which could in the combination with appropriate atomistic modeling lend themselves well for the development of a better understanding of dynamic crack instabilities [106]. Since reliable tight binding descriptions of silicon and fitting on the fly [146] are now becoming available, such studies can be expected in the near future.

Probably, the greatest open issue not only for dynamic fracture but also for the understanding of the brittle to ductile transition is the interaction of cracks and dislocations. Dislocation nucleation and multiplication at a crack tip obviously are important processes there and atomistic modeling is the only tool available right now to investigate such processes in full resolution. Experiments are scarce but the impinging of a single dislocation on a loaded crack in silicon single crystal has been studied by in situ X-ray topography and revealed massive dislocation multiplication in a very short time [151]. Such processes are very difficult to observe in any other material and should therefore be used as a starting point for the atomistic modeling.

The issues for dislocation studies are first and outmost the dislocation core properties themselves. With the focus on nanoscale systems, however, increasing attention must also be paid to the interaction of dislocations with interfaces. There, we will probably gain a lot more understanding about the role of interfaces as sources and sinks of dislocations and about the mechanisms by which slip can be transmitted across interfaces from atomistic simulations. The above mentioned studies of nanocrystals and small confined systems will in the future be able to be extended to the sizes where a transition from nanocrystalline behavior back to "normal" Hall–Petch behavior occurs [157]. At this point, systematic atomistic studies will facilitate a better understanding of nanocrystalline materials and may even suggest ways to remedy their weaknesses. Another area where large-scale exploratory atomistic simulations are urgently needed will be the study of contact formation, tribology and indentation. Starting from the formation of the chemical bonds at the contact faces, via the deformation processes in the contact area to the neck formation upon separation most elementary processes are as yet poorly understood and certainly may benefit from more intensive atomistic simulations.

A key element of the atomistic simulation of dislocations will however be to provide input to mesoscale and multiscale simulation approaches (see e.g. [158,159]). There, the interaction of dislocations with short-range obstacles certainly plays an important role. Of similar importance is the actual dynamics and the inertia of dislocations, which up to now is not included in the discrete dislocation simulations at all. The dislocation simulations are so far based on viscous laws of motion which certainly are insufficient for high speed deformation of materials in sliding contact, for the modeling of cutting processes or possibly even for many of the low temperature dislocation–dislocation and dislocation–obstacle interaction processes, for which first studies are just appearing [152]. Atomistic modeling has been used and will be used even more in the future to test ideas and assumptions about dislocation behavior, which at the end may be described by mesoscale techniques but must be based on the atomistic understanding.

Long-term "thermal" problems will continue to represent an exciting challenge for the atomistic community. These problems evidently cover too

large time-wise for molecular dynamics but could be handled by discrete dislocation dynamics [18–21] approaches, with dislocation-core-level information provided by atomistic simulations. To do this, the "thermal" behavior of individual dislocations in different structures/loading conditions needs to be predicted, and despite the recent progresses described in Section 3, a more complete database still needs to be established. Methods such as the NEBM as described in Section 3.1.3 can be applied to many more situations, such as dislocation–interstitial interactions [153], and dislocation–vacancy interactions including pipe diffusion or dislocation climb, etc. For sub-micron-scale deformation processes such as nanoindentation, the effects of time-dependent evolution of the generated dislocation structures need to be investigated. Apart from being an interesting fundamental issue [25], sub-micron-scale, time-dependent effects are known to severely affect the accuracy of the measurements of mechanical parameters such as reduced modulus and hardness by depth-sensing indentation techniques [154–156]. Metals are also known to creep orders-of-magnitude faster in the nanoindentation condition compared to the bulk condition at room temperature [154], and the reason is unknown so far.

In conclusion, it is clear that atomistic modeling has become a mainstream tool in the study of the mechanics of materials. Future opportunities abound, particularly with the current drive towards nanoscale systems. As in other areas of science, coherent and strong connections between theory, experiment and computation is the key to success.

## Acknowledgements

## References

[1] Frenkel J. Z Phys 1926;37:572.

[2] Ogata S, Li J, Yip S. Science 2002;298:807.

[3] Born M, Huang K. Dynamical theory of crystal lattices. Oxford: Clarendon, 1956.

[4] Watson GW, Parker SC. Phys Rev B 1995;52:13306.

[5] Li J, Yip S. Phys Rev B 1997;56:3524.

[6] Wang J, Li J, Yip S, Phillpot S, Wolf D. Phys Rev B 1995;52:12627.

[7] Li J, Van Vliet KJ, Zhu T, Yip S, Suresh S. Nature 2002;418:307.

[8] Van Vliet KJ, Li J, Zhu T, Yip S, Suresh S. Phys Rev B 2003;67:104105.

[9] Mishin Y, Mehl MJ, Papaconstantopoulos DA, Voter AF, Kress JD. Phys Rev B 2001;63:224106.

[10] Vitek V. Scripta Metall 1970;4:725.

[11] Chang J. PhD Thesis, Massachusetts Institute of Technology; 2003.

[12] Freund LB, Suresh S. Thin film materials: stress, defect formation and surface evolution. Cambridge University Press, 2003.

[13] Johnson KL. Contact mechanics. New York: Cambridge University Press; 1985.

[14] Kelchner CL, Plimpton SJ, Hamilton JC. Phys Rev B 1998;58:11085.

[15] Zhu T, Li J, Van Vliet KJ, Ogata S, Yip S, Suresh S. J Mech Phys Solids 2003, in press.

[16] Shenoy VB, Miller R, Tadmor EB, Rodney D, Phillips R, Ortiz M. J Mech Phys Solids 1999;47:611.

[17] Ericksen JL. In: Gurtin ME, editor. Phase transformations and material instabilities in solids. Academic Press; 1984, p. 61–78.

[18] Zbib HM, De La Rubia TD, Rhee M, Hirth JP. J Nucl Mater 2000;276:154.

[19] Devincre B, Kubin LP, Lemarchand C, Madec R. Mater Sci Eng A 2001;309–310:211.

[20] Huang J, Ghoniem NM. Model Simul Mater Sci Eng 2003;11:21.

[21] Cai W, Bulatov VV, Justo JF, Argon AS, Yip S. Comp Mater Sci 2002;23:124.

[22] Suresh S, Nieh T-G, Choi BW. Scripta Mater 1999;41:951.

[23] Gouldstone A, Koh H-J, Zeng K-Y, Giannakopoulos AE, Suresh S. Acta Mater 2000;48:2277.

[24] Li J. Modell Simul Mater Sci Eng 2003;11:173. Available from: http://alum.mit.edu/www/liju99/Graphics/A/.

[25] Chiu YL, Ngan AHW. Acta Mater 2002;50:1599.

[26] Kailer A, Gogotsi YG, Nickel KG. J Appl Phys 1997;81:3057.

[27] Smith GS, Tadmor EB, Bernstein N, Kaxiras E. Acta Mater 2001;49:4089.

[28] Vegge T, Rasmussen T, Leffers T, Pedersen OB, Jacobsen KW. Philos Mag Lett 2001;81:137.

[29] Xu W, Moriarty JA. Comp Mater Sci 1998;9:348.

[30] Bulatov VV, Kaxiras E. Phys Rev Lett 1997;78:4221.

[31] Shen C, Wang Y. Acta Mater 2003;51:2595.

[32] Seeger A. Mater Sci Eng A 2001;319-321:254.

[33] Ito K, Vitek V. Phil Mag A 2001;81:1387.

[34] Vitek V. Intermetallics 1998;6:579.

[35] Gumbsch P, Taeri-Baghbadrani S, Brunner D, Sigle W, Rühle M. Phys Rev Lett 2001;87:085505.

[36] Mills MJ, Daw MS, Foiles SM. Ultramicroscopy 1994;56:79.

[37] Inkson BJ, Humphreys CJ. Philos Mag Lett 1995;71:307.

[38] Schroll R, Vitek V, Gumbsch P. Acta Mater 1998;46:903.

[39] George A, Yip S. Scripta Mater 2001;45:1233.

[40] Cai W, Bulatov VV, Chang J, Li J, Yip S. Dislocations in solids. Hirth JP, editor. vol. 13, in press.

[41] Püschl W. Prog Mater Sci 2002;47:415.

[42] Hirsch PB. Oral communication in Fifth International Congress of Crystallography, Cambridge, 1960.

[43] Duesbery MS, Hirsch PB. In: Rosenfield AR, Hahn GT, Bement Jr. AL, editors. Dislocation dynamics. New York: Battelle Institute Materials Science Colloquia, McGraw-Hill; 1968, p. 57.

[44] Duesbery MS. Philos Mag 1969;19:501.

[45] Celli V, Kabler M, Ninomiya T, Thomson R. Phys Rev 1963;131:58.

[46] Dorn JE, Rajnak S. Trans AIME 1964;230:1052.

[47] Duesbery MS, Vitek V, Bowen DK. Proc R Soc Lond A 1973;332:85.

[48] Vitek V. Cryst Lattice Defects 1974;5:1–34.

[49] Duesbery MS. In: Nabarro FRN, editor. Dislocation in solids, vol. 8. Amsterdam, New York: North-Holland; 1989, p. 69.

[50] Suzuki T, Takeuchi S, Yoshinaga H. Dislocation dynamics and plasticity. Berlin: Springer; 1991 Chapter 6.

[51] Vitek V. Philos Mag 1968;18:773.

[52] Duesbery MS, Vitek V. Acta Mater 1998;46:1481.

[53] Suzuki T, Koizumi H, Kirchner HOK. Acta Metall Mater 1995;43:2177.

[54] Woodward C, Rao SI. Philos Mag A 2001;81:1305.

[55] Woodward C, Rao SI. Phys Rev Lett 2002;88:216402.

[56] Kroupa F, Lejcek L. Phys Stat Sol A 1975;29:K39–K41.

[57] Ngan AHW. Philos Mag Lett 1995;72:207.

[58] Ngan AHW. J Mech Phys Solids 1997;45:903.

[59] Ngan AHW. Philos Mag A 1999;79:1697.

[60] Ngan AHW, Zhang HF. J Appl Phys 1999;86:1236.

[61] Wen M, Ngan AHW. Acta Mater 2000;48:4255.

[62] Ngan AHW, Wen M. Comp Mater Sci 2002;23:139.

[63] Ngan AHW, Wen M. Phys Rev Lett 2001;87:75505.

[64] Basinski ZS, Duesbery MS, Murty GS. Acta Metall 1981;29:801.

[65] Aono Y, Kuramoto E, Kitajima K. Rep Res Inst Appl Mech, Kyushu Univ 1981;29:127, reprinted in Suzuki T, Takeuchi S, Yoshinaga H. Dislocation dynamics and plasticity. Springer: Berlin; 1991, p. 94 [Chapter 6].

[66] Brunner D, Diehl J. Phys Stat Sol A 1987;104:145.

[67] Vineyard GH. J Phys Chem Solids 1957;3:121.

[68] Mills G, Jónsson H, Schenter GK. Surf Sci 1995;324:305.

[69] Rasmussen T, Jacobsen KW, Leffers T, Pedersen OB, Srinivasan SG, Jónsson H. Phys Rev Lett 1997;79:3676.

[70] Rasmussen T, Jacobsen KW, Leffers T, Pedersen OB. Phys Rev B 1997;56:2977.

[71] Duesbery MS. Acta Metall 1983;31:1747.

[72] Paidar V, Pope DP, Vitek V. Acta Metall 1984;32:435.

[73] Hirsch PB. Prog Mater Sci 1992;36:63.

[74] Schoeck G. Phil Mag Lett 1994;70:179.

[75] Parthasarathy TA, Dimiduk DM. Acta Mater 1996;44:2237.

[76] Yoo MH. Acta Metall 1987;35:1559.

[77] Voter AF, Chen SP. Characterization of defects in materials. Siegel RW, Weertman JR, Sinclair R, editors. Mater Res Soc Symp Proc 1987;82:175.

[78] Sinclair JE, Gehlen PC, Hoagland RG, Hirth JP. J Appl Phys 1978;49:3890.

[79] Ngan AHW. Philos Mag Lett 1995;72:11.

[80] Ngan AHW. Philos Mag Lett 1994;70:121.

[81] Schroll R, Gumbsch P. Phys Stat Sol A 1998;166:475.

[82] Brunner D, Gumbsch P. Z Metallkunde 2002;93:672.

[83] Gumbsch P. Science 1998;279:1489.

[84] Zhou SJ, Preston DL, Lomdahl PS, Beazley DM. Science 1998;279:1525.

[85] Rodney D, Phillips R. Phys Rev Lett 1999;82:1704.

[86] Shenoy VB, Kukta RV, Phillips R. Phys Rev Lett 2000;84:1491.

[87] Madec R, Devincre B, Kubin LB. Phys Rev Lett 2002;89:255508.

[88] Van Vliet KJ, Tsikata S, Suresh S. Appl Phys Lett 2003;83:1441.

[89] Arzt E. Acta Mater 1998;46:5611.

[90] Schiotz J, DiTolla FD, Jacobsen KW. Nature 1998;391:561.

[91] Van Swygenhoven H, Derlet PM. Phys Rev B 2001;64:224105.

[92] Van Swygenhoven H, Derlet PM, Hasnaoui A. Phys Rev B 2002;66:024101.

[93] Yamakov V, Wolf D, Salazar M, Phillpot SR, Gleiter H. Acta Mater 2001;49:2713.

[94] Yamakov V, Wolf D, Phillpot SR, Mukherjee AK, Gleiter H. Nature Mater 2002;1:45.

[95] Abraham FF. Europhys Lett 1997;38:103.

[96] Lawn BR. Fracture of brittle solids. Cambridge, UK: Cambridge University Press, 1993.

[97] Clarke DR. In: Faber KT, Malloy K, editors. Semiconductors and semimetals. Academic Press; 1992, p. 7–9.

[98] Griffith AA. Philos Trans R Soc London, Ser A 1921;221:163.

[99] Thomson R, Hsieh C, Rana V. J Appl Phys 1971;42:3154.

[100] Selinger RLB, Farkas D. MRS Bull 2000;25/5:11.

[101] Gumbsch P, Cannon RM. MRS Bull 2000;25/5:15.

[102] Gumbsch P. In: Materials science for the 21st century, vol. A. Japan: The Society of Materials Science, JSMS; 2001, p. 50.

[103] Michot G. Crys Prop Prep 1988;17-18:55.

[104] George A, Michot G. Mater Sci Eng A 1993;164:118.

[105] Pérez R, Gumbsch P. Acta Mater 2000;48:4517.

[106] Cramer T, Wanner A, Gumbsch P. Phys Rev Lett 2000;85:788.

[107] Pérez R, Gumbsch P. Phys Rev Lett 2000;84:5347.

[108] Marder M, Gross S, Mech J. J Mech Phys Solids 1995;43:1.

[109] Gumbsch P, Zhou S-J, Holian BL. Phys Rev B 1997;55:3445.

[110] Hauch JA, Holland D, Marder MP, Swinney HL. Phys Rev Lett 1999;82:3823.

[111] Swadener JG, Baskes MI, Nastasi M. Phys Rev Lett 2002;89:085503.

[112] Mikulla R, Stadler J, Krul F, Trebin H-R, Gumbsch P. Phys Rev Lett 1998;81:3163.

[113] Holland D, Marder M. Adv Mater 1999;11:793.

[114] Rudhart C, Gumbsch P, Trebin H-R. In: Trebin H-R, editor. Quasicrystals, structure and physical properties. Weinheim: Wiley-VCH; 2003, p. 484.

[115] Falk ML, Langer JS. Phys Rev E 1998;57:7192.

[116] Falk ML, Langer JS. MRS Bull 2000;25/5:40.

[117] Gao H, Huang Y, Gumbsch P, Rosakis AJ. J Mech Phys Solids 1999;47:1941.

[118] Gumbsch P, Gao H. Science 1999;283:965.

[119] Gao H, Huang Y, Abraham FF. J Mech Phys Solids 2001;49:2113.

[120] Rice JR, Thomson R. Philos Mag 1974;29:73.

[121] Schoeck G. Philos Mag A 1991;63:111.

[122] Rice JR. J Mech Phys Solids 1992;40:239.

[123] Ngan AHW, Zhang HF. Mech Mater 1999;31:367.

[124] Zhang HF, Ngan AHW. Scripta Mater 1999;41:737.

[125] Gumbsch P, Riedle J, Hartmaier A, Fischmeister HF. Science 1998;282:1293.

[126] Qiao Y, Argon AS. Mech Mater 2003;35:129.

[127] Ebrahimi F, Shrivastava S. Acta Mater 1998;46:1493.

[128] Hartmaier A, Gumbsch P. J Comput-Aided Mater Des 1999;6:145.

[129] Hirsch PB, Roberts SG. Philos Mag A 1991;64:55.

[130] Serbena FC, Roberts SG. Acta Metall Mater 1994;42:2505.

[131] Hartmaier A, Gumbsch P. Philos Mag A 2002;82:3187.

[132] Wang CZ, Pan BC, Ho KM. J Phys—Condensed Matter 1999;11:2043.

[133] Qiu SY, Wang CZ, Ho KM, Chan CT. J Phys—Condensed Matter 1994;6:9153.

[134] Horsfield AP. Mater Sci Eng B 1996;37:219.

[135] Pettifor DG, Horsfield AP, Nguyen Manh D, Aoki M, Gumbsch P, Vitek V. Mater Sci Eng A 1995;192–193:24.

[136] Haas H, Wang CZ, Fähnle M, Elsässer C, Ho KM. Phys Rev B 1998;57:1461.

[137] Girshick A, Bratkovsky AM, Pettifor DG, Vitek V. Philos Mag A 1998;77:981.

[138] Znam S, Nguyen-Manh D, Pettifor DG, Vitek V. Philos Mag A 2003;83:415.

[139] Nguyen-Manh D, Pettifor DG, Cockayne DJH, Mrovec M, Znam S, Vitek V. Bull Mater Sci 2003;26:43.

[140] Kohlhoff S, Gumbsch P, Fischmeister HF. Philos Mag A 1991;64:851.

[141] Gumbsch P. J Mater Res 1995;10:2897.

[142] Ortiz M, Phillips R. Adv Appl Mech 1999;36:1.

[143] Broughton JQ, Abraham FF, Bernstein N, Kaxiras E. Phys Rev B 1999;60:2391.

[144] Abraham FF, Bernstein N, Broughton JQ, Hess D. MRS Bull 2000;25/5:27.

[145] De Vita A, Car R. Tight-binding approach to Comp Mater Sci. Turchi PEA, Gonis A, Colombo L, editors. Mater Res Soc Symp Proc 1998;473:473.

[146] Trimarchi G, Albaret T, Gumbsch P, Meriani S, Barth J, De Vita A. Computational modelling and simulation of materials II. In: Proc of CIMTEC. 2002, p. 35.

[147] Tong Q-Y, Gösele U. Science and technology of semiconductor wafer bonding. J. Wiley & Sons, 1999.

[148] Bagdahn J, Knoll H, Wiemer M, Petzold M. Microsys Technol 2003;9:204.

[149] Suwito W, Dunn ML, Cunningham SJ, Read DT. J Appl Phys 1999;85:3519.

[150] Lehmann G, Lomonosov AM, Hess P, Gumbsch P. J Appl Phys 2003;94:2907.

[151] Scandian C, Azzouzi H, Maloufi N, Michot G, George A. Phys Stat Sol A 1999;171:67.

[152] Osetsky YN, Bacon DJ. Modell Simul Mater Sci Eng 2003;11:427.

[153] Wen M, Fukuyama S, Yokogawa K. Acta Mater 2003;51:1767.

[154] Feng G, Ngan AHW. J Mater Res 2002;17:660.

[155] Ngan AHW, Tang B. J Mater Res 2002;17:2604.

[156] Tang B, Ngan AHW. J Mater Res 2003;18:1141.

[157] Schiotz J, Jacobsen KW. Science 2003;301:1357.

[158] Madec R, Devincre B, Kubin L, Hoc T, Rodney D. Science 2003;301:1879.

[159] Gumbsch P. Science 2003;301:1857.